

# Reconstructing the Salgar 2015 Flash Flood Using Radar Retrievals and a Conceptual Modeling Framework: A Basis for a Better Flood Generating Mechanisms Discrimination

Nicolás Velásquez <sup>1,2</sup>, Carlos D. Hoyos <sup>1,2</sup>, Jaime I. Vélez <sup>1</sup>, and Esneider Zapata <sup>2</sup>

<sup>1</sup>Universidad Nacional de Colombia, Sede Medellín, Facultad de Minas, Departamento de Geociencias y Medio Ambiente

<sup>2</sup>Sistema de Alerta Temprana de Medellín y el Valle de Aburrá (SIATA)

*Correspondence to:* Nicolás Velásquez (nvelasqg@unal.edu.co)

**Abstract.** During May 18 of 2015, severe rainfall triggered a flash flood in the municipality of Salgar, located in the northwestern Colombian Andes. This work aims to reconstruct the main features of the flash flood to understand better the hydrological processes modulating the event occurrence. Radar quantitative precipitation estimates (QPE), satellite data, and post-event field visits are used

- 5 to reconstruct the Salgar flash flood addressing the relationship between rainfall spatio-temporal structure, soil moisture, and runoff generation during successive rainfall events, using a conceptual modeling framework including land-slide and hydraulic sub-models. The hydrologic model includes virtual tracers to explore the role of runoff and subsurface flow, as well as the relative importance of convective and stratiform precipitation in flash flood generation. In spite of potential shortcomings,
- 10 the modeling results allow an assessment of the impact of the interactions between runoff, subsurface flow, and convective-stratiform rainfall on the short-term hydrological mechanisms leading to the flash flood event. The overall methodology reproduces considerably well the magnitude and timing of La Liboriana flash flood discharge peak, as well as the areas of landslide occurrence and flood spots, with some limitations due to the digital elevation model spatial resolution. Simulation results
- 15 indicate that the flash-flood and the regional land-slide features were strongly influenced by the antecedent rainfall associated with a northeasterly stratiform event that recharged the gravitational and capillary storages within the model. The simulation shows that the antecedent rainfall event moistens the entire basin before the occurrence of the flash flood event, modulating as well the streamflow during the flash flood event. Evidence suggests that the spatial structure of the rainfall is
- 20 at least as important as the geomorphological features of the basin in regulating the occurrence of flash flood events.

## 1 Introduction

Flash floods are regarded as one of the most destructive hydrological hazards resulting in considerable loss of human life and high costs due to infrastructure damage (Roux et al., 2011; Gruntfest and 25 Handmer, 2001). Among all different types of floods, Jonkman (2005) shows that flash floods result in the highest average mortality rate per event (3.62%), almost ten times larger than the mortality rate for river floods. Flash floods are usually described as rapidly rising water level events happening in steep streams and rivers, associated with short-term, very intense convective precipitation systems, or orographically forced rainfall events over highly saturated land surfaces and steep terrains (Šálek 30 et al., 2006; Llasat et al., 2016; Douinot et al., 2016). Convective precipitation episodes often feature high intensity, short duration, and relatively reduced spatial coverage (Houze, 2004).

Several authors have assessed the role of the geological and geomorphological features of the catchment, soil type, soil moisture conditions, and the spatio-temporal structure of rainfall on flash 35 flood occurrence, trying to identify the leading causative mechanisms of this hazard (Merz and Blöschl, 2003). Adamovic et al. (2016) and Vannier et al. (2016) tried to understand the governing processes of flash floods from the geological formation of the basin with mixed results. Wu and Sidle (1995) emphasize the role of the topography, ground cover, and groundwater in the occurrence 40 of shallow landslides and associated debris flows. Due to their rapid nature, flash floods are more likely to occur in small and steep basins (Younis et al., 2008); many authors have assessed the influence of hills and stream slopes suggesting the slopes of the hills are significantly more important for flash floods occurrence and magnitude than the slope of the stream (Šálek et al., 2006; Roux et al., 2011; Yatheendradas et al., 2008). Rodriguez-Blanco et al. (2012) analyzed fifty-four flash 45 flood episodes in Spain and determined that antecedent soil moisture conditions play a vital role in runoff production. Castillo et al. (2003), using a modeling approach, also suggested an important flash flood occurrence dependence on antecedent moisture conditions. Aronica et al. (2012) used spatial and statistical analysis to reconstruct landslides and deposits, finding a connection between flash flood occurrence and soil moisture antecedent conditions.

50 The fact that small basins are more prone to flash floods increases their intrinsic physical and measurement uncertainty (Wagener et al., 2007), difficulting their prediction (Hardy et al., 2016; Ruiz-Villanueva et al., 2013; Yamanaka and Ma, 2017; Borga et al., 2011; Marra et al., 2017), and underlining the need for high spatio-temporal resolution precipitation data (Norbiato et al., 2008). Given the critical role of precipitation, some authors follow a climatological approximation to assess 55 the recurrence of flash floods in particular regions, focusing on the atmospheric causative mechanisms. For example, Kahana et al. (2002) examined the extent to which floods in the Negev Desert are the outcome of climatological synoptic-scale features finding that about 80% of the events can be linked to distinct synoptic conditions days prior the flood events. Schumacher and Johnson (2005)

studied extreme rain events associated with flash flooding in the United States over a 3-yr period  
60 using the national radar reflectivity composite data to examine the structure and evolution of each extreme rain events. The use of radar data to study flash flood generating storms is vital for understanding and forecasting these events (National Research Council 1996). Schumacher and Johnson (2005) found that 65% of the total number of episodes are associated with mesoscale convective systems (MCSs), with two recurrent patterns of organization: the existence of training convective elements and the generation of quasi-stationary areas of convection with stratiform rainfall downstream. Fragoso et al. (2012) analyzed storm characteristics and required rainfall conditions for flash flood occurrence at Madeira (Portugal), and their results suggest an essential role of global climate patterns (North Atlantic Oscillation -NAO- forcing) and also local forcing (orographic features) in the triggering of such events. Implicitly, these studies and all the others available in the peer-reviewed  
65 literature point to the need for local and regional high-quality spatio-temporal rainfall data. Berne and Krajewski (2013) highlight the need to incorporate high-resolution weather radar information, even with some limitations, in flash flood hydrology.

The topography of Colombia is characterized by three branches of the Andes crossing the country  
75 south-to-north, generating a mixture of landscapes from high snow-capped mountains, vast highland plateaus, deep canyons to wide valleys, making some regions highly prone to flash flood occurrence. The likelihood of flash flood occurrence in Colombia is also high due to the spatio-temporal behavior of the Intertropical Convergence Zone, and the direction of the near-surface moist air flow leading to orographic enhancement of convective cores (Poveda et al., 2007). In the last decade, there have  
80 been several widespread and localized flash flood events in Colombia associated with climatological features and with the local intensification of rainfall events. The 2010-2011 La Niña event alone triggered 1233 flooding events and 778 mass removal processes in Colombia, with more than 3 million people affected and damages estimated by the "Comisión Económica para América Latina y el Caribe" in more than 6.5 billion US dollars.

85

After the 2010-2011 widespread disaster, several isolated events have occurred in the country with devastating consequences. The present paper focuses on studying the processes triggering a flash flood in La Liboriana basin, a  $56 \text{ km}^2$  basin located in the western range of the Colombian Andes, as a result of consecutive rainfall storms that took place between May 15th and May 18th, 2015.  
90 The resulting flash flood dramatically affected the region, causing more than 100 casualties, affecting several buildings and critical infrastructure, and resulting in a total reconstruction cost estimated at 36.000 million Colombian pesos (approximately 12,5 million dollars considering 2018 exchange rate), which corresponds to three times the annual income of the municipality. Figure 1 shows an example of infrastructure damage as a result of the flash flood event, and changes of the basin's main  
95 channel after the flash flood, showing considerable river margin and bed erosion. In spite of the data



a) Aerial photograph before the event (2012).



b) Aerial photograph taken after the event (2015-05).

**Figure 1.** Example of infrastructure damage as a result of the La Liboriana May 18 of 2015 flash flood event. a) Aerial photograph before the event (2012) taken during a mission of the Department of Antioquia's Government, and b) satellite image after the event (2015-05). The images show the destruction of most houses  at that particular community, a bridge over La Liboriana, and the main road. The images also present changes in the delineation of the main channel as well as considerable erosion in the river margins.

scarcity, including discharge measurements, the analysis of the successive rainfall events triggering the Salgar flash flood provide an interesting case of study for assessing the mechanisms depending on the soil moisture conditions and rainfall distribution.

100 La Liboriana basin flash flood is a typical case of prediction in ungauged basins (Sivapalan et al., 2016; Seibert and Beven, 2009; Beven, 2007; Bonell et al., 2006; Yamanaka and Ma, 2017). In this case, there are no local records of soils or land use and the local hydro-meteorological data is scarce or non-existent and certainly not available in real time. Due to the lack of data, La Liboriana case imposes a challenge for flash flood prediction and modeling  according to Blöschl et al. (2012),  
 105 there are three methods for using models in these cases. The first strategy is to obtain the required

model parameters from historical basin behavior and the morphological characteristics of the basin. This strategy often leads to low model performance (Duan et al., 2006). The second approach is to inherit the hydrological calibration from a gauged neighboring watershed, which in this case does not exist. The third method is to parameterize the model based on proxy variables, such as hydraulic  
110 information obtained during field visits. In the case of the 2015 La Liboriana basin flash flood, there are no previous historical streamflow records, nor records from a neighboring watershed, thus we followed the third approach. In this work, we use precipitation information derived from radar, satellite and aerial images, and post-event field visits to reconstruct the Salgar flash flood event. This study addresses two broad hydrological issues. The first issue consists in exploring the relationship  
115 between rainfall spatio-temporal structure (Llasat et al., 2016; Fragoso et al., 2012), soil moisture and runoff generation (Penna et al., 2011; Tramblay et al., 2012; Garambois et al., 2013) during the successive rainfall events, and the second issue in proposing a simplified hydrologic modeling scheme including land-slide and hydraulic sub-models to assess the potential occurrence of flash flood events.

120

The methodology followed in this study makes use of a conceptual modeling framework that includes a hydrologic model (Vélez, 2001; Francés et al., 2007a), a shallow land-slide sub-model (Aristizábal et al., 2016), and a hydraulic sub-model (hereafter referred to as HydroFlash). The hydrologic model includes virtual tracers to explore separately the role of runoff and subsurface flow,  
125 as well as the relative importance of convective and stratiform precipitation in flash flood generation. The assessment of the interactions between runoff, subsurface flow, and convective-stratiform rainfall allows a better understanding of the short-term hydrological mechanisms leading to the flash flood event. A comparison between the results from both sub-models and the observed landslides scars and flooded spots helps to evaluate the overall skill of the proposed methodology.

130

The document is structured as follows. Section 2 describes in more detail the region of study, La Liboriana basin, including geomorphological and climatological characteristics of the basin as well as the information sources used in this study. Section 3 presents a description of the overall methodology and the model used for the reconstruction of the 2015 La Liboriana flash flood event,  
135 including flow separation, shallow landslide parameterization, and the proposed hydraulic model. Section 4 describes the main results of the study, including model validation and sensitivity analysis, and presents results from the land-slide and inundation sub-models. Section 5 includes a discussion on the role of the rainfall structure in the flash flood reconstruction. Finally, the conclusions are presented in section 6.

140 **2 Study Site and Data**

**2.1 Catchment description**

The urban area of Salgar municipality is located near the outlet of La Liboriana basin, a small (56 km<sup>2</sup>) tropical watershed located in the westernmost range of Colombia's Andes (Figure 2). By 2015, the population of Salgar was estimated at 17400 persons, 8800 residing in the urban area. La Libo-  
145 riana basin joins El Barroso river basin and both drain to Cauca river.

The availability of the ALOS-PALSAR Digital Elevation Model (DEM) (ASF, 2011), with a resolution of about 12.7 m, allows estimating the fundamental geomorphological features of the basin. The average slope of La Liboriana is 57.6 %, and the basin longitude and perimeter are 13.5 km  
150 and 57.8 km, respectively. The Strahler-Horton order of the main stream is 5, and its longitude and slope are 18.1 km and 8.1 %, respectively. The highest elevation of the watershed (Cerro Plateado) reaches 3609 meters above sea level (m.a.s.l), while the outlet of the basin is at 1316 m.a.s.l.. The 99th slope percentile of order 1 streams is 78%. For streams order 2, 3, 4, and 5, the 99th slope percentile are 61, 27, 18 y 11%, respectively. Figure 2 shows the spatial distribution of the slopes in  
155 the watershed. These features are typical of Andean mountainous basins. Geomorphologically, this kind of watershed tends to be prone to the occurrence of flash floods (Lehmann and Or, 2012; Penna et al., 2011; Martín-Vide and Llasat, 2018; Longoni et al., 2016; Ozturk et al., 2018; Khosravi et al., 2018; Marchi et al., 2016; Bisht et al., 2018).

160 At the sub-basin scale, La Liboriana exhibits a vast range of slopes and altitude differences. Figure 2 shows the Height Above the Nearest Drainage -HAND- model (Rennó et al., 2008) for La Liboriana. The HAND calculates the relative difference between cell *i* and its nearest streamflow cell *j*. La Liboriana HAND exhibits values between 500 and 800 m. Near the outlet of the basin, over the banks, there are values close to 0 m. High HAND values at the upper region of the water-  
165 shed often denote areas of high potential energy, with increased sediment production and frequent shallow landslide occurrence. Banks with low HAND values are more susceptible to flooding and tend to correspond to areas prone to extensive damages caused by extreme events. While the elevation differences described in Figure 2 are typical of the region, the social challenges lie in the high vulnerability of Salgar given the location of the main urban settlement.

170

Vegetation and land use vary considerably within the basin. Figure 3 shows land use in different regions of the watershed from a 2012 aerial image. In the upper La Liboriana basin, there is dense vegetation (see Zoom 1 in Figure 3), with a high percentage of tropical forests, with the presence of grass and few crop fields. A portion of the upper watershed is considered a national park. Hillslopes  
175 near the divide do not evidence significant anthropic intervention most likely due steepness of this

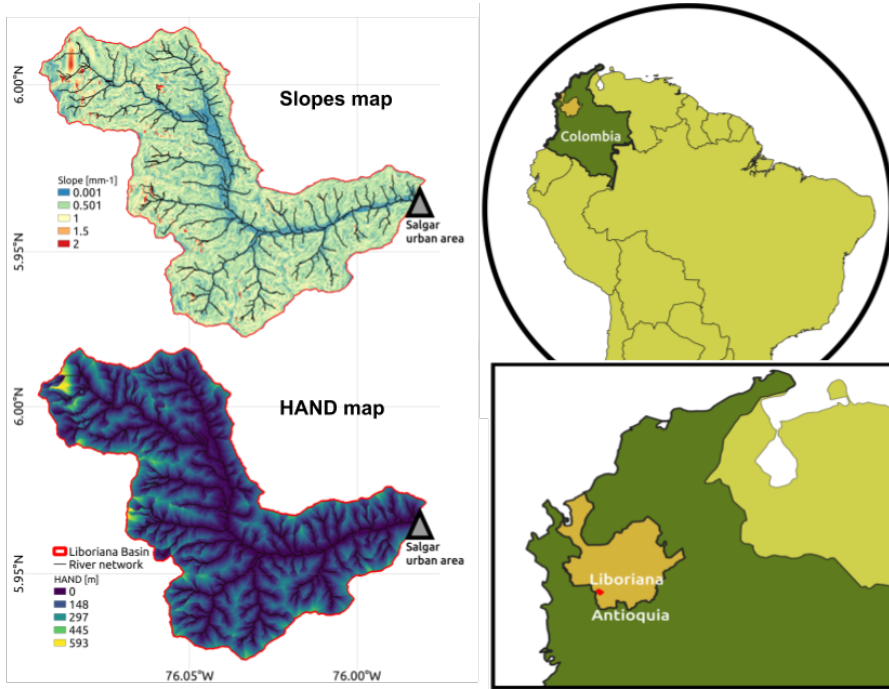


**Figure 2.** Geographical context of Liboriana basin, located in Colombia, in the Department of Antioquia. The color bar represents the Height Above the Nearest Drainage (HAND). HAND values were estimated using the same resolution of the DEM (12.7 m). Low HAND values correspond to areas prone to flooding.

region. Down the hills and at the bottom of the valley there are coffee plantations (the primary economic activity of the region) and pastures. Downstream (Figure 3, Zoom 2), it is evident the presence of crops among forest and grass. Near the middle of the basin (Figure 3, Zoom 3), the presence of crops is more notorious and human settlements and roads start to appear. The watershed exhibits 180 grazing areas and urban development near the river banks. In Figure 3, Zoom 4, corresponding to the first affected urban area from upstream to downstream during the flash flood, it is also possible to see a marked presence of crops and some forest patches. Finally, zoom 5 shows the main urban area of Salgar surrounded by crops, grass and an important loss of forest coverage.

185 One of the challenges for hydrological modeling and risk management in the country is that soils are not well mapped; the national soil cartography is usually available in a 1:400.000 scale. At this scale, the municipality of Salgar, including La Liboriana basin, corresponds to only one category of soil texture. Osorio (2008), based on field campaign observations and laboratory tests, described La Liboriana soils as a well-drained soil with poor retention capacity. Organic material is predominant 190 in the first layer and clay loam soil within the second one. The depth of the soil is hillslope dependent, varying from 20cm to 1m (Osorio, 2008). Table 1 provides a summary of soil characteristics for five different categories, all as a function of slope. Each soil category has a corresponding depth

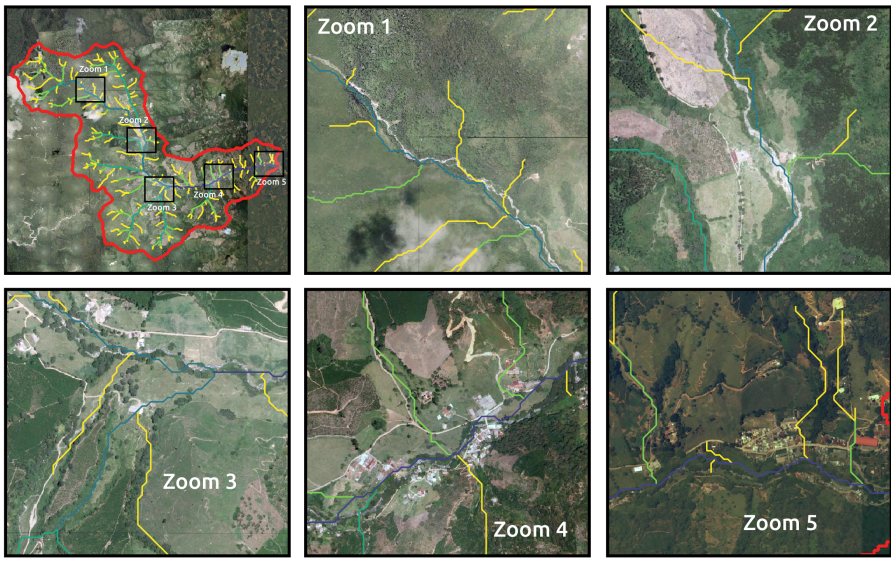


**Figure 3.** Land use in different regions of La Liboriana watershed from a 2012 aerial images (Source: Department of Antioquia).

**Table 1.** Description of the soils in the region (Osorio, 2008).

| Type              | Slope | Depth [m] | Retention | Permeability |
|-------------------|-------|-----------|-----------|--------------|
| <b>Class III</b>  | 12-25 | 0.6       | Mean      | Mean         |
| <b>Class IV</b>   | <12   | 0.6       | Low       | High         |
| <b>Class VI</b>   | 25-30 | 1.0       | Mean      | Mean         |
| <b>Class VII</b>  | 30-50 | 0.3       | Too Low   |              |
| <b>Class VIII</b> | >50   | 0.2       | Too Low   | Slow         |

and a qualitative description of permeability and retention.

## 195 2.2 Flash flood post-event observations

We conducted a field campaign a few days after the May 18th flash flood event to assess cross-section geometry along the main channel in different sites, including at the outlet of the basin. Unfortunately, most of the affected areas were not accessible after the event and it was not possible to obtain reliable information in other locations along the main channel other than at the outlet of the basin. During 200 the campaign, we measured sectional distances and surface water speed different points of the streamflow. We also identified traditional post-event terrain, land-cover, vegetation and infrastructure markers to assess the high-water marks associated with the peak of the flash flood. Figure 4 presents



**Figure 4.** Channel cross-section shown an example of flooded infrastructure after the flash flood event. The section shows mud marks on the walls with heights varying between 0.5 and 1.2 m. These mud stains are evident in buildings located 4-5 m away from the channel. The photograph also shows the width of the channel and the total estimated depth during the flash flood.

the selected cross-section used for the estimation of the maximum discharge during the flash flood given its geometrical and hydraulic regularity. The section has a rectangular shape, 4.6 m wide and 205 a height of 5 m for a total area of about  $23 \text{ m}^2$ . A visual inspection of the flooded house around the section, located 4-5 m away from the channel, reveals the presence of mud marks on the walls with heights varying between 0.5 and 1.2 m (see Figure 4). The area of the section plus the flooded area during the event was estimated to be approximately  $37 \text{ m}^2$ . During the campaign we measured 210 surface speeds in the channel oscillating between 2 and 3  $\text{m s}^{-1}$ . In instrumented basins in the region, with similar characteristics in terms of area and slopes, we have recorded peak flow surface water 215 speeds oscillating between 5 and 7  $\text{m s}^{-1}$ . By assuming an area of  $37 \text{ m}^2$  and the mentioned surface speeds, we estimate that the observed flash flood peak flow may have been between 185 and 222  $\text{m}^3 \text{s}^{-1}$ . The timing of the peak flow is also important information. Local authorities reported that the peak streamflow reached the urban perimeter after 2:10 a.m. May 18th. Some reports state that 220 the peak flow in the most affected community occurred around 2:40 a.m.

There is also relevant aerial information before and after the occurrence of the event. During 2012, the Department of Antioquia conducted a detailed aerial survey of the Salgar municipality, and few 225 days after the event Google  released publicly high detailed satellite images of the same region. The contrast between both products provides information about flooded areas and landslide locations. Field campaign estimates and aerial imagery are central to validate the results obtained from 230 the proposed models.

## 2.3 Rainfall Information

225 The assessment of the 2015 Salgar flash flood event following a hydrological modeling strategy uses a radar-based QPE technique developed by Sepúlveda and Hoyos (2019) using rainfall gauges and disdrometers within the radar domain to obtain spatiotemporal precipitation maps over the basin. A detailed description of the rainfall estimation, as well as the overall meteorological conditions that led to the La Liboriana extreme event, are described in a companion paper (Hoyos et al. 2019).

230 The QPE technique uses retrievals from a C-band polarimetric Doppler weather radar operated by the Sistema de Alerta Temprana de Medellín y el Valle de Aburra (SIATA, a local early warning system from a neighboring region, [www.siata.gov.co](http://www.siata.gov.co)), located around 90 km away from the basin. The radar has an optimal optimum range of 120 km radius for rainfall estimation and a maximum operational range of 240 km for weather detection. The radar operating strategy allows obtaining

235 precipitation information every 5 minutes with a spatial resolution is about 128 m. The results of the radar QPE methodology indicate that the rainfall estimation works well within a radius of 120km. Despite the distance between the radar and the basin, and the mountains between them, there are no blind spots for the radar. A comparison between the radar QPE estimates and records from two rain gauges installed three days after the flash flood event show a correlation for an hourly time scale of

240 0.65. In addition to the rainfall quantification, radar retrievals, before feeding the hydrologic model, are classified in convective and stratiform areas following a methodology proposed by Houze et al. (2015) and Steiner et al. (1995) 

245 Between May 15th and May 18th, 2015, several storms took place over La Liboriana basin. During the night of May 17th, between 02:00 and 09:00 a.m. (local time), a precipitation event covered almost all the basin (hereafter referred to as precipitation Event 1). Twenty hours later, between 23:00 p.m. of May 17 and 02:00 a.m. of May 18 two successive extreme convective systems occurred over the basin with the maximum intensity in the upper hills (precipitation Event 2). Event 1 corresponds mainly to a stratiform event, covering almost all the basin area and with an average

250 precipitation accumulation of 47 mm  Event 2 accumulated, in average over the basin, around 38 mm, however over the upper watershed the accumulation exceeded 180 mm  Figure 5a presents the temporal evolution of the convective-stratiform rainfall partitioning during both Events 1 and 2. The main difference between both events is the timing of the convective versus stratiform participation within each case. Event 1 started as a stratiform precipitation event moving from the southwest, from the Department of Chocó to the Department of Antioquia across westernmost Andes mountain range. Chocó is the雨iest department in Colombia, and one of the wettest places on Earth, due to the inflow of moisture from the Pacific Ocean and the orientation of the Andes mountain range (Poveda and Mesa, 2000; Mapes et al., 2001)  After 3 hours of stratiform rainfall, training convective cores move over La Liboriana basin generating intense precipitation peaks during 2.5 hours.

255 It is important to note that these cores did not strengthen within La Liboriana basin; these systems

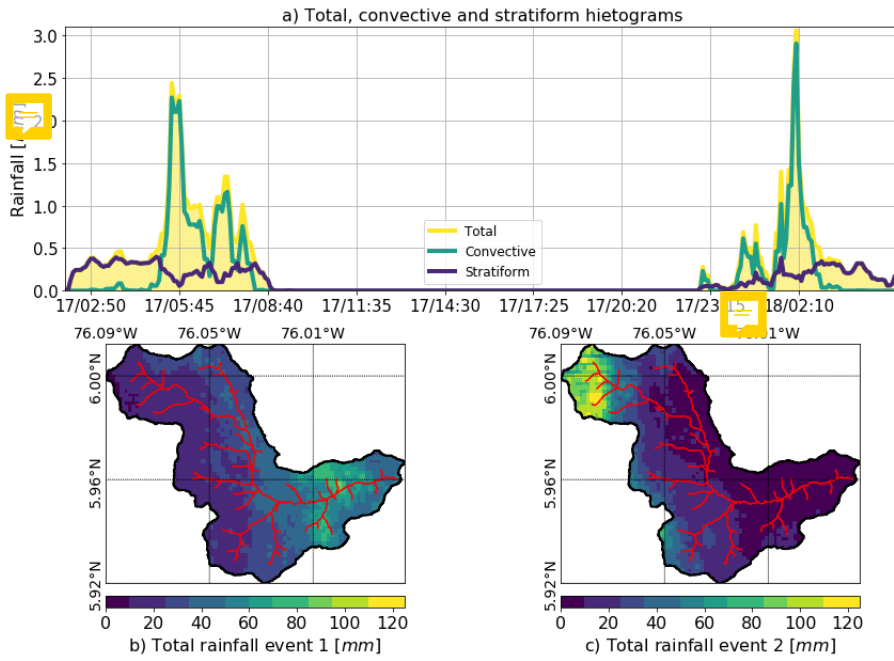


**Figure 5.** a) Temporal evolution of the convective-stratiform rainfall partitioning during both Events 1 and 2. The figure shows the total rainfall (yellow), and the convective (blue) and stratiform (green) portions integrated over La Liboriana basin. b) and c) Spatial distribution of the cumulative rainfall during Events 1 and 2 over La Liboriana basin.

formed and intensified over the western hills of Farallones de Citará draining to the Department of Chocó towards the Atrato river. The latter is not a minor fact because once the convective system moved with a northeast direction, the maximum intensity cores did not fall over the steepest hills of La Liboriana basin but rather near the basin outlet where the slopes are considerably flatter. Figure 265 5b shows the spatial distribution cumulative rainfall during Event 1, with the maximum precipitation located towards the bottom third of the basin. Event 2, on the other hand, started as a thunderstorm training event with two convective cores moving from the southeast followed by remaining stratiform precipitation. Even though the average cumulative rainfall over the basin was 9 mm less than during Event 1, this event is characterized by orographic intensification within the basin leading to a 270 more heterogeneous spatial distribution and with the highest cumulative precipitation in the steepest portion of the basin (see Figure 5b). Event 2 spatial distribution and highly localized observed intensities most likely led to the flash-flooding episode, as it is explored in this work.

The data requirements, and rainfall preprocessing needed for the overall methodology followed in 275 the reconstruction of the 2015 Salgar flash flood are summarized in Table 2 and are presented in a schematic diagram in Figure 6.

| Item              | Description  | Period                   | Usage   |
|-------------------|--|--------------------------|---|
| Radar data        | QPE rainfall estimations   | 2015-05-17 to 2015-05-18 | Hydrologic model runs. Rainfall characterization and event analysis.  |
| Field campaign    | Maximum streamflow estimation through visual inspection          | 2015-05-20               | Hydrologic model comparison for indirect validation.  |
| Satellite imagery | Visible channel compositions from the Digital Globe CNES imagery | 2015-05 (post-event)     | Flash flood model validation, shallow land-slides model validation, and comparison with pre-event conditions. |
| Aerial photos     | Aerial photos taken by the government of Antioquia during 2012.  | 2012                     | Pre-event conditions comparison.  |
| Soils description | Physical description of the soils of the region by Osorio (2008) | 2008                     | Hydrologic model setup.   |

**Table 2.** Summary of the data used for the model setup.

### 3 Methodology

#### 3.1 Hydrological modeling framework

280 The availability of radar-based QPE and a detailed DEM allows the use of a modeling framework based on the distributed hydrologic model described in Vélez (2001) and Francés et al. (2007a) with important modifications. The hydrologic model simulates different hydrological processes as independent, but interacting storages (second row, left panel in Figure 6). The model distributes processes by cells; in each cell  tanks represent the hydrological processes including capillary (tank 1), gravitational (tank 2), runoff (tank 3), baseflow (tank 4) and channel storage (tank 5). The state of each tank varies in function of vertical and lateral flows as shown in the diagram, where the storage is represented by  $S_i$ , the vertical input to each tank by  $D_i$ , which in turns depends on the vertical flow through tanks  $R_i$ .  $E_i$  represents the downstream connection between cells, except for tank 1, where  $E_1$  represents the evaporation rate. Vertical flows are only time dependent, while lateral flows 285 could also depend on the actual state of the tank (kinematic approximation).

290

The model modifications fall in four different categories: (i) the direct use of radar QPE as a source of rainfall information, (ii) the implementation of virtual tracers for surface and subsurface discharge as well as for convective and stratiform water tracing, (iii) the enforcement of a maximum 295 gravitational storage ( $H_g$ ) to allow Hortonian runoff (return flow from  $S_3$  (tank 3) to  $S_2$  (tank 2)), and (iv) the development of two modules for hazard assessment. The implementation of virtual trac-

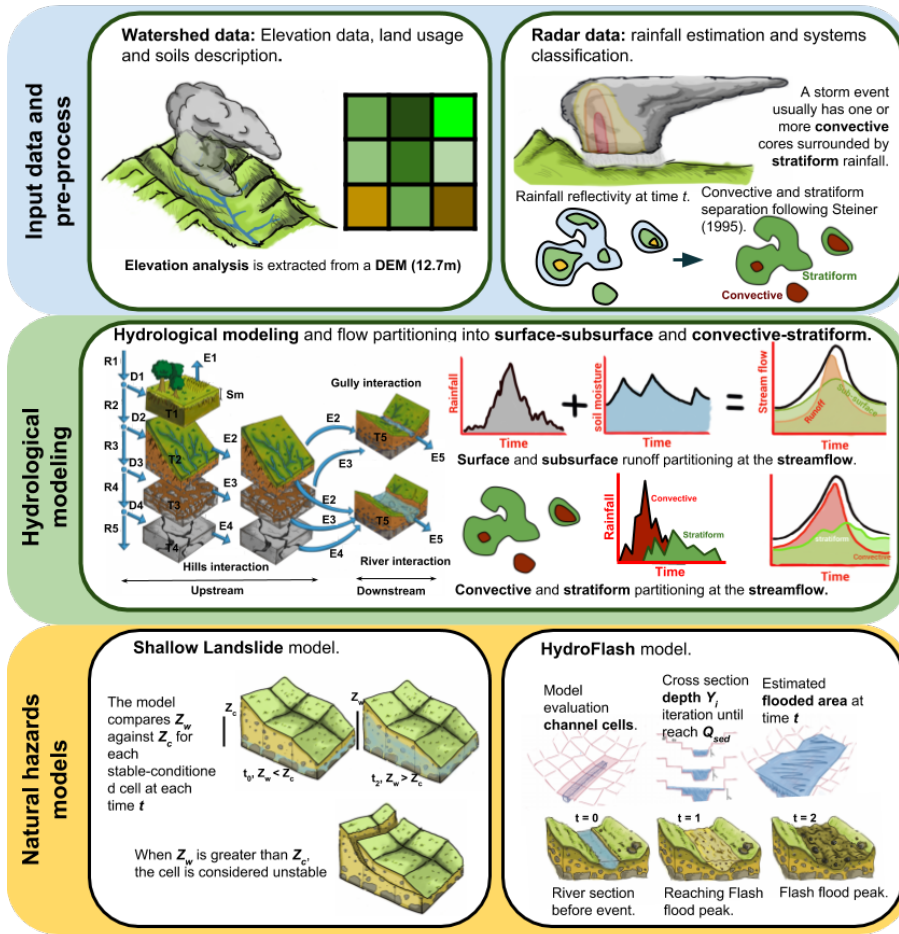


**Figure 6.** Illustrative diagram of the methodology followed in the present study. The top row represents the availability of a detailed DEM and radar-based QPE as the basis of the modeling framework. The second row represents the mains aspects of the distributed hydrologic model used. In each cell five tanks represent the hydrological processes including capillary (tank 1), gravitational (tank 2), runoff (tank 3), baseflow (tank 4) and channel storage (tank 5). The state of each tank varies in function of vertical and lateral flows as shown in the diagram, where the storage is represented by  $S_i$ , the vertical input by  $D_i$  which in turns depends on the vertical flow through tanks  $R_i$ .  $E_i$  represents the downstream connection between cells, and evaporation. The implementation of convective and stratiform rainfall separation and virtual tracers is also portrayed. The implementation of the shallow landslides model and HydroFlash are schematized in the bottom row.

ers is represented in the top two right panels of the diagram in Figure6.

### 3.1.1 Hydrological runoff scheme modification

300 In the model, horizontal flow equations could be either linear or potential, as shown in equation 1. In the modified hydrologic model,  $\beta$  and  $\alpha$  are estimated by the user and then set into the model. In

the non-lineal approximation  $\beta$  is a coefficient that summarizes local properties invariant over time, like the slope or the hydraulic conductivity.  $\alpha$  is an exponent that change in function of the adopted approximation. From equations 1 to 3,  $A_i(t)$  corresponds to the sectional area of each storage,  $A_i(t)$

305 vary in function of the tank storage  $S_i(t)$  according to equation 4.

$$v_{tank}(t) = \beta A_i(t)^\alpha \quad (1)$$

Non-linear equations in lateral flows could result in a better representation of processes at high resolutions (Beven, 1981; Kirkby and Chorley, 1967). A non-linear approximation to runoff is presented in equation 2. This approximation is a modification of Manning's formula for flow in gullies.

310 According to Foster G.R. (1984),  $\varepsilon$  and  $e_1$  are a coefficient and an exponent used to translate the manning channel concept into multiple small channels or gullies. The values of  $\varepsilon$  and  $e_1$  are 0.5 and 0.64, respectively (Foster G.R., 1984).  $A_2$  is the corresponding sectional area obtained from  $S_2$  by using the equation (4). And  $S_0$  is the slope of the cell.

The non-linear equation 3 corresponds to an adaptation of Kubota and Sivapalan (1995) formula 315 for subsurface runoff where  $k_s$  is the saturated hydraulic conductivity, and the exponent  $b$  is dependent on the soil type, assumed equal to 2.  $A_g$  is the equivalent cross-section area to the maximum gravitational storage ( $H_g$ ).  $A_3$  is the corresponding sectional area of the gravitational storage ( $S_3$ ) obtained by using equation (4). There is also return flow from tank 3 to tank 2 when  $S_3 = H_g$ , representing runoff generation by saturation.

$$320 \quad v_2 = \frac{\varepsilon}{n} S_0^{1/2} A_2(t)^{(2/3)e_1} \quad (2)$$

$$v_3 = \frac{K_s S_0^2}{(b+1) A_g^b} A_3(t)^b \quad (3)$$

The equations describe the momentum of a kinematic wave approximation. In both cases, velocity depends on the tank storage. These relations are summarized in equation 1, that could be solved 325 numerically coupled with a mass balance equation (equation 4). This equation takes into account the storage at each time step ( $S_{tank}(t)$ ), the longitude of the element ( $\Delta x$ ), the time step size ( $\Delta t$ ), and the speed estimated for the flow in the time step ( $v_{tank}(t)$ ). Equation 4 is related to equation 1 through the velocity term for that tank ( $v_{tank}$ ) and the cross-sectional area of the tank ( $A_{tank}$ ). The solution to  $v_{tank}$  and  $A_{tank}$  is obtained through an iterative scheme. The total outflow from the tank 330 is calculated using equation 5.

$$A_i(t) = \frac{S_{tank}(t)}{\Delta x + v_{tank}(t)\Delta t} \quad (4)$$

$$E_{tank}(t) = A_{tank}(t)v_{tank}(t)\Delta t \quad (5)$$

### 3.1.2 Virtual Tracers

335 Virtual tracers are implemented into the model to discriminate streamflow source in superficial runoff and subsurface flow and to assess the portion of streamflow from convective rainfall and stratiform precipitation, recording at each time step and each cell the source of water. The model archives the results of the virtual tracing algorithm at the outlet of the basin and at each reach allowing the study of the role of flows from different nature during extreme events at different spatial scales to get more  
340 insights about the soil-driven flow regulation.

The flow separation module operates in tanks 2 (runoff storage) and 3 (subsurface storage). The module marks water once it reaches any of those two tanks and the runoff-subsurface flow percentage are taken into account once the water enters tank 5 (the channel). At this point, the scheme 345 assumes that the water in the channel is well mixed, implying that the flow percentage is constant until a new inflow enters the channel.

With a similar concept, the model also follows convective and stratiform rainfall. For this, at each time step, the model takes into account the rainfall classified as convective or stratiform, and assumes that at each particular cell the precipitation is either entirely convective or entirely stratiform. This assumption could lead to estimation errors at basins represented by coarse cells (low DEM resolution) where convective and stratiform precipitation are likely to coexist. In the present study the spatial resolution of the DEM is 12.7m, higher than the resolution of the radar retrievals (about 355 12m), so the potential convective and stratiform rainfall concurrence is very low, and it could not be identified using the Steiner et al. (1995) approach.

### 3.1.3 Hydrologic model calibration

The hydrologic model requires a total of ten parameters. Table 3 includes all the parameters used in the model. The values of the parameters were derived from the soil properties described in section 360 2. Due to the lack of detailed information in the region, parameters such as the infiltration and percolation rates are assumed as constant in all the basin. Other parameters such as the capillary and gravitational storage vary in function of geomorphological characteristics of the basin such as the elevation and slope. According to Francés et al. (2007b), during the calibration process, each 365 physical parameter is scaled by a constant value in the entire basin. Table 3 includes the mean value for all the parameters used in the model and the scalar value adjusted during the model calibration.

| Parameter Name        | Symbol     | Scalar    | Mean Value  | Spatial distribution                                      |
|-----------------------|------------|-----------|---|---|
|                       |            | Parameter |   |   |
| Capillary storage     | Hu [mm]    | 1         | 39  | In function of the slope                                  |
| Gravitational storage | Hg [mm]    | 1         | 34  | As a function of the slope                                |
| Evaporation rate      | Etr [mm/s] | 0.1       | 0.01  | As a function of the DEM                                  |
| Infiltration rate     | ks [mm/s]  | 2.7       | 0.0012   | Lumped  |
| Percolation rate      | kp [mm/s]  | 0.8       | 0.00012  | Lumped  |
| System losses         | Kf [mm/s]  | 0         | 0.0   | Lumped  |
| Surface speed         | vr [m/s]   | 0.5       | 6.4      | As a function of the slope and storage                    |
| Subsurface speed      | vs [m/s]   | 1         | 7.1   | As a function of the slope, Hg and storage                |
| Subterranean speed    | vb [m/s]   | 0.5       | 0.000095  | Lumped  |
| Channel speed         | vc [m/s]   | 1         | 0.95  | As a function of the slope, accumulated area, and storage |

**Table 3.** Hydrologic model parameters

### 3.2 Shallow landslides sub-model

The shallow landslides submodel coupled to the hydrologic model is proposed by Aristizábal et al. The submodel classifies cells into three groups: unconditionally stable, conditionally stable and unconditionally unstable. Figure 7 describes the variables of the model and the balance of forces considered. Three parameters determine stability of each cell: (i) residual soil thickness water table  $Z_{i,min}$  estimated as in equation 6, (ii) the maximum soil depth at which a particular soil remains stable  $Z_{i,max}$  estimated as in equation 7, and (iii) the maximum slope at which the soil remains stable  $\beta_{i,0}$  estimated as in equation 8. In the equations and in the Figure 7  $\gamma$  is the soil bulk density,  $\gamma_w$  is the water density,  $Z_w$  is the saturated soil thickness above the slip surface,  $Z$  is the soil thickness measured vertically,  $\beta$  is the gradient of the hillslope, and  $\phi$  is the soil stability angle.  $Q_L$  and  $Q_R$  are the resultant forces on the sides of the slice.

$$Z_{i,min} = \frac{C'}{\gamma_w \cos^2 \beta \tan \phi + \gamma \cos^2 \beta (\tan \beta - \tan \phi)} \quad (6)$$

$$Z_{i,max} = \frac{C'}{\gamma \cos^2 \beta (\tan \beta - \tan \phi)} \quad (7)$$

$$\beta_{i,0} = \tan^{-1} \left[ \tan \phi \left( 1 - \frac{\gamma_w}{\gamma} \right) \right] \quad (8)$$

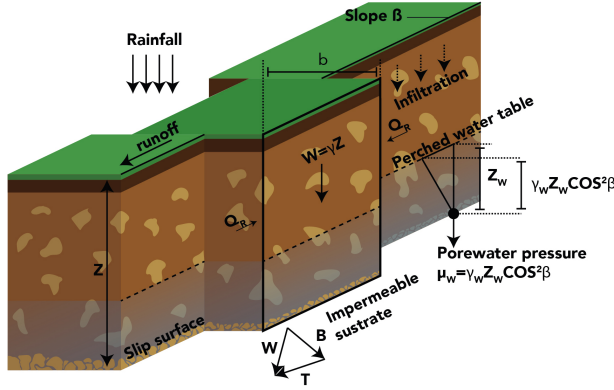


**Figure 7.** The geotechnical conceptual model. Figure and description are adapted from Aristizábal et al. (2016).

The model assess conditionally stable cells in function of their perched water table for each cell ( $Z_{i,w}$ , equation 9) and the critical saturated depth ( $Z_{i,c}$ , equation (10)). Slope failure occurs when  $Z_{i,w}$  is greater than  $Z_{i,c}$ . At equation (9)  $S_{3,t}$  represents gravitational storage,  $W_s$  and  $W_{fc}$  the soil 385 saturation and field capacity respectively. And in equation (10)  $C'$  represents the soil cohesion and  $\beta$  the cell slope.

$$Z_{i,w}(t) = \frac{S_{3,t}}{W_c - W_{fc}} \quad (9)$$

$$Z_{i,c} = \frac{\gamma}{\gamma_w} Z \left( 1 - \frac{\tan \beta}{\tan \phi} \right) + \frac{C'}{\gamma_w \cos^2 \beta \tan \phi} \quad (10)$$

### 390 3.3 Flash flood submodel (HydroFlash)

In this work, we introduce a low-cost 1D hydraulic model for flash flood simulation referred to as HydroFlash. The model extracts the cross-profile from the DEM for each cell considered part of the network, estimating flood spots at each network cell during execution time.

395 The model requires hydraulic parameters for all network cells to determine flash-flooding spots. Channel width is estimated using the Leopold (1953) approach  $W_i = 3.26 C^{0.469}$ . Channel slope ( $S_{i,0}$ ) is obtained as the mean value of the slopes that correspond to the cells of a hydrological reach. The characteristic particle diameter  $D_{i,5}$  is assumed equal to 0.138m and constant (Golden and 400 Springer, 2006). The cross-section ( $C_s$ ) is obtained from the DEM, for every network cell, perpendicular to the flow direction of the cell ( $D_{8i}$ )

For each time step  $t$  and for each stream cell, equation 11 determines the height of the water table  $Y_i(t)$  using the simulated streamflow  $Q_{i,sim}(t)$  and flow velocity  $v_{i,sim}(t)$ . The model calculates

the friction velocity ( $v_{fr,i}(t)$ ) using  $Y_i(t)$  as in equation (12) derived from Keulegan and Rouse equations (Takahashi, 1991; Savage and Sayed, 1984). Equations 13 and 14 allow the estimation of the concentration ( $c_i(t)$ ) and constitutive coefficients ( $r_i(t)$ ), respectively. In equation 13  $C_{max}$  represents the maximum sediment concentration; according to Obrien (1988)  $C_{max}$  is near 0.75 during flash floods. The stream flow plus estimated sediments and rubble is estimated according to equation 15.

$$410 \quad Y_i(t) = \frac{Q_{i,sim}(t)}{v_{i,sim}(t)w_i} \quad (11)$$

$$v_{fr,i}(t) = \frac{v_{i,sim}(t)}{5.75 \log \left( \frac{Y_i(t)}{D_{i,50}} \right) + 6.25} \quad (12)$$

$$c_i(t) = C_{max} (0.06 Y_i(t))^{\frac{0.2}{v_{fr,i}(t)}} \quad (13)$$

415

$$r_i(t) = \frac{1}{D_{i,50}} \left[ \frac{g}{0.0128} \left( c_i + (1 - c_i) \frac{\gamma_w}{\gamma_{sed}} \right) \right]^{1/2} \cdot \left[ \left( \frac{C_{max}}{c_i} \right)^{1/3} - 1 \right] \quad (14)$$

$$Q_{i,sed}(t) = \frac{Q_{i,sim}(t)}{1 - c_i(t)} \quad (15)$$

Assuming infinite sediment and rubble supply,  $Q_{i,sed}(t)$  is the maximum stream flow for the section. To determine the flooded area, a flood depth  $F_{d,i}(t)$  must be found in order to obtain an stream flow ( $\hat{Q}_{i,sed}(t)$ ) (equation 18) that equals  $Q_{i,sed}(t)$ . The search of  $F_{d,i}$  is done iteratively by making small increments to it. Both flooded area ( $A_{i,sed}(t)$ ) and flooded section ( $F_{f,i}$ ) are obtained in the process. At each iteration,  $F_{d,i}$  is an estimated depth (equation 16), measured from the bottom of the section ( $b_i$ ) to a guess elevation of the section ( $\Delta y \cdot j$ ). The depth of  $F_{d,i}$  increases with each iteration as  $j$  takes values between 1 and the total number of iterations with a step of 1. At the end of each iteration,  $A_{i,sed}(t)$  is estimated with equation 17, in which  $F_{sec,i}$  corresponds to the section  $i$  extracted from the DEM. Based on the value obtained for  $A_{i,sed}(t)$ , the model estimates  $\hat{Q}_{i,sed}$  (equation 18). The process stops when  $\hat{Q}_{i,sed}$  is similar to  $Q_{i,sed}$ , at this point, the flooded section  $F_{f,i}$  corresponds to the values of  $F_{sec,i}$  that are below  $F_{d,i}$  

$$430 \quad F_{d,i} = b_i + \Delta y \cdot j \quad (16)$$

$$\hat{A}_{i,sed} = \Delta x \sum_{j=1}^N F_{d,i} - F_{sec,i} \quad (17)$$

$$\hat{Q}_{i,sed}(t) = \left(\frac{2}{5}\right) r_i(t) (j \Delta y)^{\frac{3}{2}} S_{0,i} \hat{A}_{i,sed}(t) \cdot 0.5 \quad (18)$$

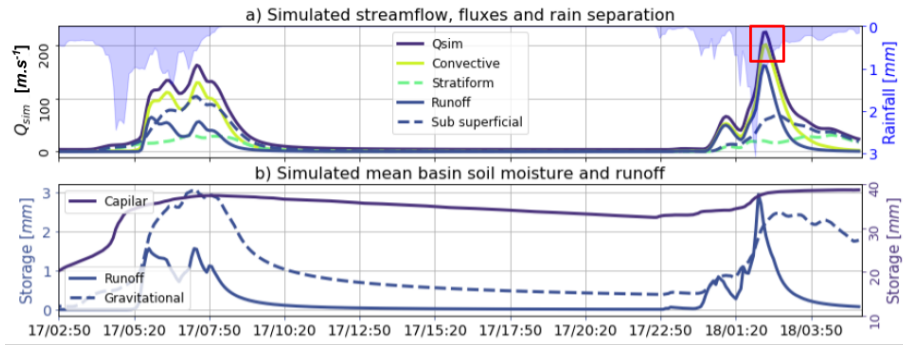
Resulting flood maps might evidence the presence of small isolated flood spots and discontinuities at flood spots where flow direction changes from orthogonal to diagonal or vice-versa. We included  
 435 two post-processing steps to correct these issues by (i) using an image processing erosion algorithm (Serra, 1983) to remove the small isolated flood spots. The erosion is performed once with a 3x3 kernel, and (ii) to solve the flow direction discontinuities, each flooded cell seeks to flood its eight neighboring cells. A neighbor cell is also flooded if the altitude of the original flooded cell plus the flood depth is higher than its elevation. 

440 **4 Results**

The primary results of the present study include the reconstruction of the 2015 Salgar flash flood, the assessment of the importance of soil moisture in the hydrologic response of the basin, and the evaluation of the relative role of stratiform and convective precipitation cores in the generation of the observed extreme event. This section is based on the results from the analysis of the hydrological  
 445 simulation, as well as shallow landslides and flash floods occurrence and simulation.

#### 4.1 Hydrologic model validation and sensitivity analysis

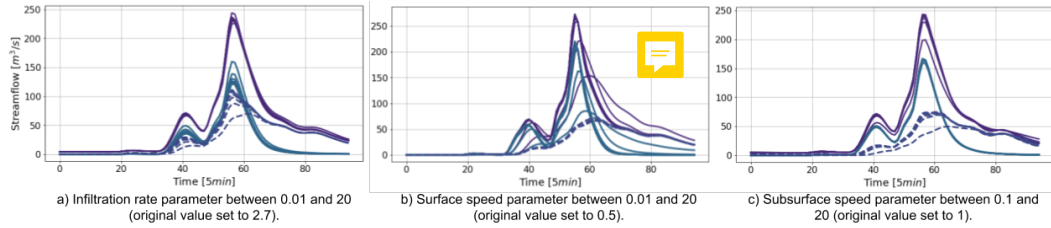
Figure 8a presents the results of the hydrological simulation at the outlet of the basin. The model simulation is set to reach a base flow of  $3 \text{ m}^3 \text{s}^{-1}$   value that corresponds to the discharge measurements during field campaigns days and weeks after the flash flood event and during dry spells. The  
 450 simulation shows that Event 1 generates a hydrograph with a peak flow of  $Q_{max} = 160 \text{ m}^3 \text{s}^{-1}$ . It is important to note that during precipitation Event 1 there were no damage nor flooding reports by local authorities  even though this precipitation event did not generate flooding, it set wet conditions in the entire basin before the occurrence of Event 2 (see the purple line in Figure 8b). Additionally, it is clear from the simulation that during the flash flood event the two successive convective  
 455 cores over the same region (training convection) generated a peak flow of  $Q_{max} = 220 \text{ m}^3 \text{s}^{-1}$ , value that is in the upper range of the estimated streamflow based on post-event field evidence (185-222  $\text{m}^3 \text{s}^{-1}$ ). Figure 8a also presents the simulated runoff and subsurface flow separation as well as the convective-stratiform generated discharge discrimination. The modeling evidence during Event 2  
 460 suggests the convective rainfall fraction dominates the hydrograph formation. In both events, convective (stratiform) precipitation appears to be closely related to the simulated runoff (subsurface flow). On the other hand, the simulated subsurface flow is more important in magnitude than runoff in describing Event 1, while runoff is more relevant for Event 2. Figure 8b presents capillary stor  

**Figure 8.** Summary of the Results from the hydrological simulation. a) Simulated streamflow, runoff and subsurface flow separation and convective-stratiform generated discharge discrimination. The red square represents the flash flood peakflow interval estimated based on field campaing evidence. b) Mean runoff, gravitational, and capillary storages during the simulation period.

(purple), as well as runoff (continuous blue) and gravitational (dashed blue) storage temporal variability. As expected, runoff storage is only non-zero during the storm duration, while gravitational storage increases considerably during rain events, followed by a slow recession. There is an increment of basin-wide capillary storage during Event 1, remaining considerably high the time leading to the occurrence of Event 2. According to the model simulations, the peak flow occurred around 2:20 a.m. on May 18th, which is very accurate compared to the reports from local authorities considering all the data limitations.

Figure 9 shows the results of a sensitivity analysis of the hydrological simulation during the second rainfall event, varying the infiltration rate, and the surface and subsurface speed parameters. The aim of the sensitivity analysis is to evaluate the robustness of the overall results, considering the fact that the quality and quantity of some of the watershed information is limited. The overall simulation sensitivity results show the main findings described in the previous paragraphs are, in fact, robust to almost all changes in the mentioned parameters, with surface runoff associated with convective rainfall controlling the magnitude of the peak discharge during the Event 2. Changes in the infiltration rate (Figure 9a) result in peak flow changes with a magnitude less than 7%, and changes in the subsurface velocity parameter (Figure 9c) lead to peak flow changes with a magnitude less than 20% the original simulation. The model highest sensitivity, and hence the largest uncertainty source, appears to be related to the surface speed parameter (Figure 9b), particularly in the low-end values. Although some of the surface speed values used in the analysis are unrealistically low, it is noteworthy to report that these values lead to the attenuation of the hydrograph and the reduction of the peak flow.



**Figure 9.** Hydrological simulation sensitivity analysis. Similarly as in Figure 8, all panels show the simulated streamflow, and the runoff and sub-surface flow separation. The left panel shows sensitivity to changes in the infiltration rate parameter, the middle panel to changes in surface speed, and the right panel to changes in subsurface speed.

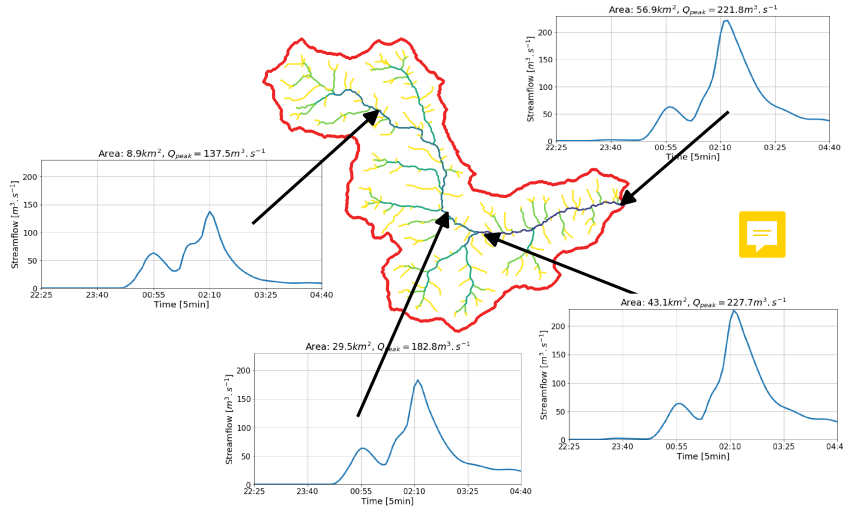


**Figure 10.** Temporal evolution of discharge during Event 2 in different locations along the watershed's main channel. The upper location corresponds to 15% of the area of the basin, and the other downstream locations to 52%, 76%, and 100% of the watershed, respectively.

Figure 10 shows the temporal evolution of discharge during Event 2 in different locations along the watershed's main channel. The upper location corresponds to 15% of the area of the basin, and the other downstream locations to 52%, 76%, and 100% of the watershed, respectively. In terms of volume, 73 Mm<sup>3</sup> of the total 144 Mm<sup>3</sup> simulated at the outlet of the basin are generated on the 15% upstream part of the watershed, corresponding to about half of the total mass. In terms of peak flow, due to the slope and velocity changes, the simulated discharge at the 15% upstream part of the watershed corresponds to 61% of the peak discharge at the outlet of the basin.

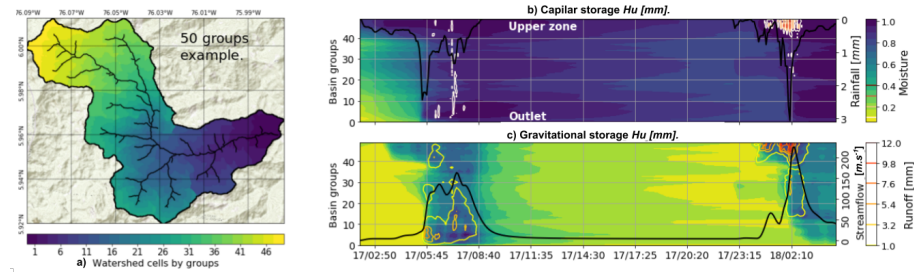


**Figure 11.** Watershed groups and spatiotemporal analysis of Events 1 and 2. a) Example of watershed grouping as a function of their localization and distance to the outlet for La Liboriana basin using a 50-groups categorization. Each group corresponds to a row in the contour plots b) and c). b) Simulated capillary moisture (filled green-to-blue contours) and returned flow occurrence (white to red isolines). The black line represents the average rainfall over the basin. c) Simulated gravitational moisture (filled green-to-blue contours) and runoff (yellow-to-red isolines). The black line represents streamflow at the outlet of the basin. The green-to-blue color bar serves as a reference for capillary moisture and gravitational water content.

495 **4.2 Flash flood processes**

In this study, we propose a graphical method to assess the soil-rainfall-discharge coupling holistically. The first step is to classify all the cells within the watershed in a predetermined number of groups according to their localization and the distance to the outlet. The aim is to establish a coherent and robust spatial discretization, thus allowing to summarize the concurrent spatio-temporal 500 variability of the different processes in 2D diagrams.

Figure 11 presents the proposed 2D diagrams obtained for the simulation of the La Liboriana basin flash flood using a spatial discretization with 50 groups. Figure 11a includes the evolution of the average rainfall over the basin (black line), and the spatio-temporal evolution of capillary storage 505 (filled isolines) and return flow (colored isolines from white to red) by groups. For the analysis, it is relevant to highlight that higher numbered groups are located away from the outlet of the basin and correspond in this case to considerably steeper slopes. Figure 11b presents the evolution of streamflow at the outlet of the basin (black line) as well as the gravitational storage (filled isolines) and runoff (colored isolines) spatio-temporal evolution. Figure 11 shows variations in the capillary and 510 gravitational storages associated with Event 1 in the higher numbered groups. The capillary storage remains high in almost all the basin until the start of Event 2. According to the conceptualization of the model, the gravitational storage and surface runoff start to interact when the capillary storage is full. In this case, this situation is set up by Eve  Model runs for Event 2 using dry initial states, show no flooding in the results.

515

It is well known that the temporal variability of rainfall intensity plays an important role in the hydrograph structure. During Event 1 rainfall accumulated over the basin at a relatively stable rate (Figure 12a). On the other hand, Event 2 presents a significant increase in rainfall rate in the second half of the life cycle (Figure 12b). This change in precipitation intensity is associated with a considerable intensification of the training convective cores due to orographic effects. Events 1 and 2 also exhibit differences in the elapsed time between rainfall occurrence and streamflow increment given the relative timing of stratiform versus convective rainfall (see the gray band in Figure 12a and b). For Event 1, the median elapsed time between rainfall and streamflow ( $Et_{p50}$ ) is 1.12 hours  while for Event 2  $Et_{p50}$  is 0.79 hours . The median elapsed time between the convective portion and the streamflow ( $Etc_{p50}$ ) in Event 1 is 0.75 and 0.46 in Event 2. The minimum value of the convective elapsed time  $Etc_{min}$  also descends from 0.42 to 0.25 hours. On the other hand, there is an increase of median elapsed time between stratiform rainfall and streamflow ( $Ets_{p50}$ ) from 1.21 to 1.83 hours. In Event 2, the convective rainfall and the runoff show a similar evolution, denoting a strong influence of the convective portion (Figure 12b).

530

As mentioned before, average rainfall accumulation over the basin for Events 1 and 2 is 47mm and 38mm  respectively. During Event 1 (2), convective (stratiform) average accumulations are 28 (23) and 17 (14) mm, respectively (Figure 13a and b). The maximum rainfall intensities are relatively similar with 150mm/h and 180mm/h for Events 1 and 2, respectively. Despite this, Event 535 1 does not trigger a flash flood event. The overall evidence suggests that the discriminating factor between both events does not lie in the portions of convective or stratiform rainfall but rather in their spatial distribut

Figures 13a and b, and Figures 13c and d show the convective and stratiform cumulative rainfall, 540 and the spatially-averaged convective and stratiform rainfall, both as a function of sub-basin reach, respectively. Figures 13a and b show that while Event 1 exhibit similar convective and stratiform rainfall accumulation for different watershed scales, Event 2 shows a more significant cumulative contribution of convective rainfall than of stratiform precipitation. Convective rainfall tends to cover less area, and at the same time present a spatio-temporal erratic behavior (Steiner et al., 1995; Houze, 545 1989). Figures 13c and d provide evidence that convective rainfall present higher variations at small sub-basins than for a larger-order basin. During Event 2, convective accumulation reaches higher values for small and medium sub-basins. Convective rainfall occurrence at the upper sub-basins has significant implications due to geomorphological conditions associated to zero-order sub-basins (Sidle et al., 2018). Figure 14 presents Pearson correlations coefficients between the convective and 550 stratiform hydrograph portions and the runoff and subsurface flow. According to this, convective and stratiform rainfall exhibit a weaker relationship with the flow characteristics at small scales (under 5km<sup>2</sup>). This is likely to be associated with increasing variability of rainfall and hydrograph forma-

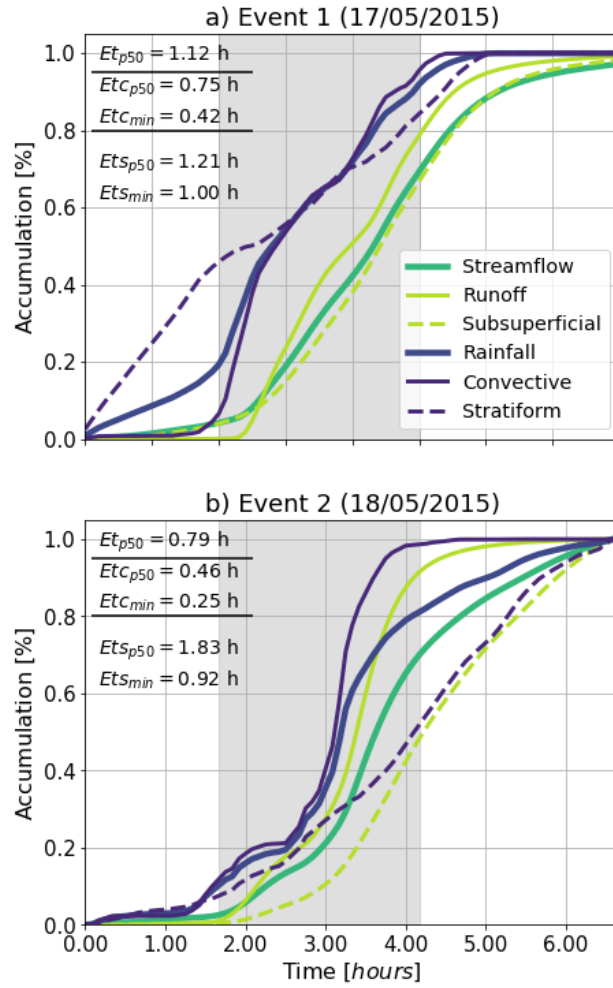


**Figure 12.** Accumulated rainfall and streamflow for a) Event 1 and b) Event 2. The accumulation is expressed in percentage respect to the total value in each case. Median elapsed time and minimum elapsed time () are estimated between total ( $Et_{p50}$ ,  $Et_{min}$ ), convective ( $Et_{c50}$ ,  $Et_{cmin}$ ), and stratiform ( $Et_{s50}$ ,  $Et_{smin}$ ) rainfall and the runoff portion of the streamflow. Gray bands correspond to the periods for elapsed time estimation.

tion at small scales (Ayalew et al., 2014). Correlations tend to grow with increasing area, indicating stabilization of the hydrograph formation. Additionally, subsurface flow presents higher correlations  
 555 during Event 1, while correlations with runoff are higher for Event 2, highlighting the most important process in each case. The relevance of subsurface flow is likely due to the rainfall characteristics during Event 1, with homogeneous rainfall intensity and high rate of basin recharge (see Figure 8b). On the other hand, saturation processes and a wet soil profile explain the observed higher correlations during Event 2.

560

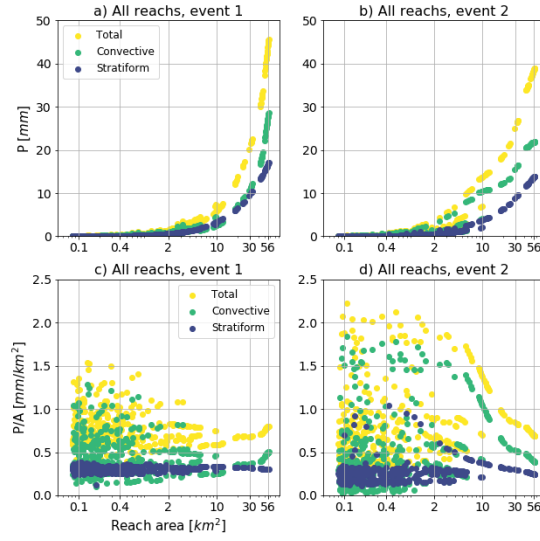


**Figure 13.** Cumulative rainfall versus the area at each reach of the basin for a) Event 1 and b) 2. Panels c) and d) show the average rainfall versus the area at each reach of the basin. Yellow dots correspond to the total, green dots to convective and blue dots to stratiform rainfall. All panels use a logarithmic scale for the basin area.

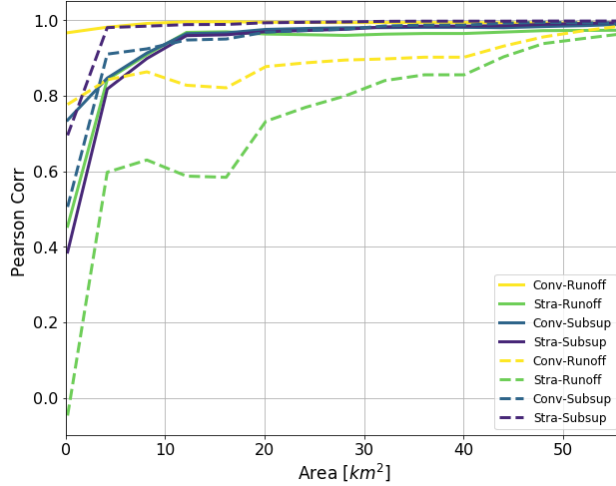


**Figure 14.** Pearson correlations among convective and stratiform portions of the rainfall and runoff and subsurface flow for different reach areas. Dashed lines correspond to Event 1 and continuous lines Event 2.

#### 4.3 Landslide and flood simulations

In addition to the hydrological simulation, associated hazards such as floods and landslides are also modeled and discussed in this study. The landslides model as described in the previous section

requires additional information including soil depth  $Z$ , cohesion  $C'$ , friction angle  $\phi$  and specific weight  $\gamma$ . According to the description by Osorio (2008), illustrating a clay-slime soil,  $C'$  is assumed equal to  $4KN$ ,  $\phi$  to  $30^0$  and  $\gamma$  to 18;  $Z$  vary with slope according to Table 1.

Figure 15a presents the observed landslides triggered by Event 2 based on aerial photos and satellite images (Landsat/Copernicus, and Google) taken before and after the flash flood. Figure 15b shows, by hills, the map of total unstable cells during the simulation period, and Figure 15c shows the time series of the number of simulated unstable cells during Event 2 (continuous purple line) and the mean rainfall over the basin (inverse axes, blue line). Calibration of the landslide model was performed by finding the maximum overlap between simulated and observed unstable and stable cells, and at the same time reducing the overall number of false positives and false negatives. It is important to note that the calibration strategy is not a cell-by-cell modification of the parameters involved but rather a basin-wide modification of soil properties. A sensitivity analysis of soil parameters is carried out by making small variations of the variables within specified intervals:  $\phi$  between 25 and 32,  $\gamma$  between 17 and 19,  $C'$  between 3.5 and 4.2, and  $Z$  between 0.1 and 3 m. The sensitivity analysis suggests that slight variations in the parameter in  $Z$  produce significant changes in the modeled landslides, resulting in an overestimation of the number of unstable cells, or no unstable cells at all. Following Table 1, the average soil depth in the basin is only 0.3 m, a value that corresponds to underestimation according to the inspections during field visits. For this reason, the results presented in Figure 15 use a  $Z$  map scaled by a calibration factor of 3.5, preserving the spatial dependence on the slope, but achieving a more realistic soil depth and better spatial distribution of landslide occurrence.

The model represents considerably well the spatial distribution of the areas that are prone to trigger shallow landslides during Event 2, showing a significant density of unstable cells in the hills where slides took place. However, despite the calibration efforts, the total number of unstable cells is relatively low compared to observations. It is important to note that there was no spatial calibration in order to obtain the right location of the landslides. The calibration only includes the change of the soil depth using a single scalar, constant for the entire basin, in order to maximize the number matching observed and simulated slides. In other words, there is just one single basin-wide parameter modified, and not an independent modification of the parameter for every pixel in order to obtain the right distribution. This is important because in that sense, it serves to check the capability of the model to estimate risk areas only considering topography and rainfall data. A pinpoint localization of the unstable cells is still considered a hard task in part due to the small temporal and spatial scale at which landslide processes take place (Aristizábal et al., 2016; Dhakal and Sidle, 2004; Wu and Sidle, 1995). Additionally, the lack of detailed soil information increases the simulation uncertainty. Notwithstanding the difficulties, the results suggest that the model simulations could have been used and should be used in the future for early detection and warning to improve both short and long-term

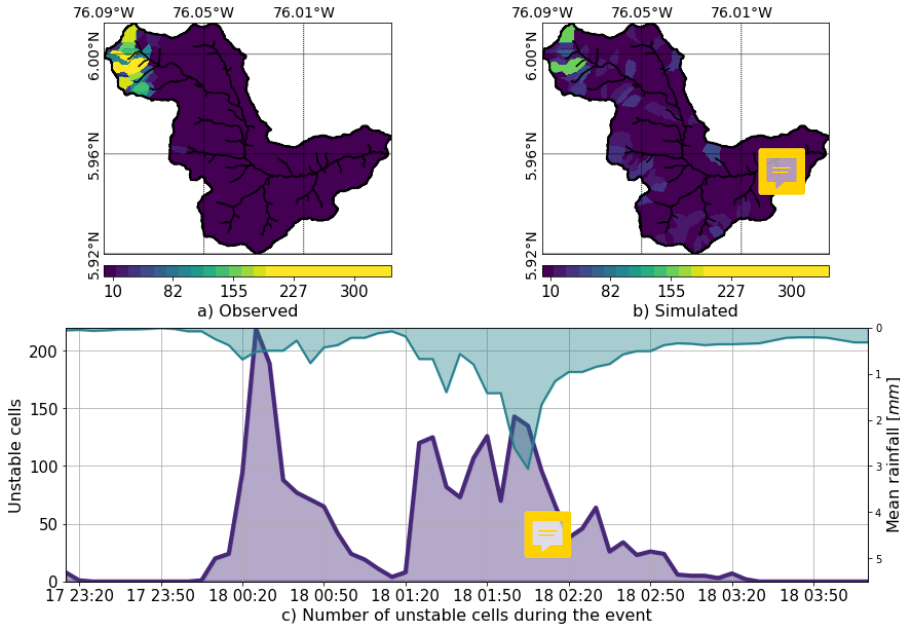


**Figure 15.** a) Observed landslides triggered by Events 1 and 2. The figure is based on aerial photos and satellite images (Landsat/Copernicus, and images available on Google) taken before and after the flash flood event. b) Map of total unstable cells during the simulation period. c) Time series of number of simulated unstable cells during Event 2 (continuous purple line) and mean rainfall over the basin (inverse axes, blue line).

risk reduction strategies.

Figure 16 shows the identification of the flood spots at the peak of Event 2 (May 18th, 2015, 2:00 a.m.) as simulated using HydroFlah. Figures 16b to f present a detail view of the results from the outlet of the basin to the upper region. Cases presented in Figures 16e and f exhibit a satisfactory agreement with observed flood spots (blue shadow). Cases in Figures 16c and d also show a good approximation, but with minor spatial shifts in some sections. The largest spatial differences are observed in Figures 16b. At the entrance of the urban zone, the model overestimates the flood spots. The model results indicate that 11% of flood spots happen at elements of order 1 and 2, and, 18, 38 and 32% happen at orders 3, 4 and 5, respectively. This also highlights a coherent geomorphological representation of the flooded channels and hills with the order.

## 5 Discussion

During the morning of May 18th of 2015, a flash flood occurred in the steep La Liboriana basin, in the municipality of Salgar, Department of Antioquia, Colombia, leaving more than 100 human casualties, 535 houses destroyed, and significant infrastructure loses. Due to the lack of local in-

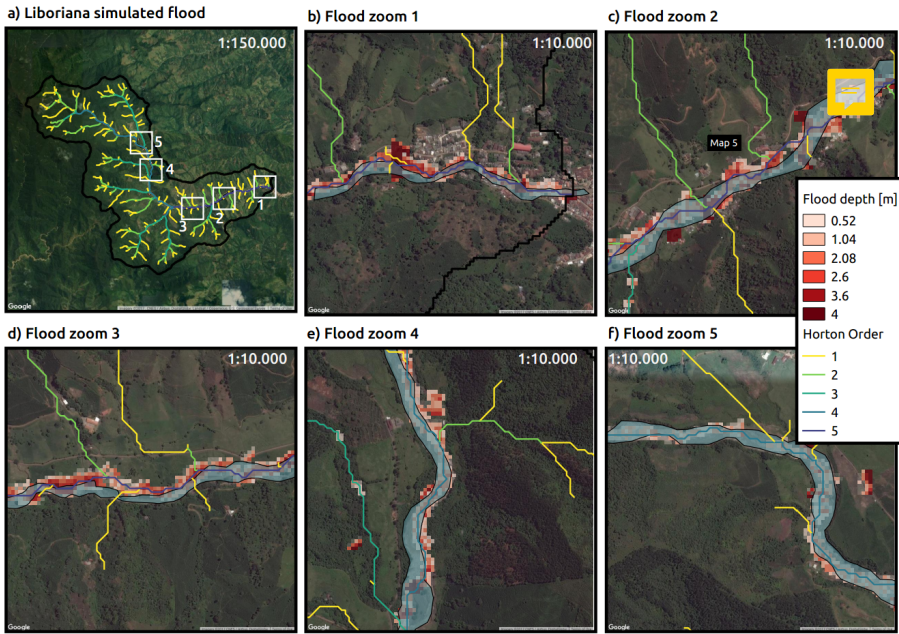


**Figure 16.** Simulated flood spot at the peak of Event 2 in different locations. a) Basin drainage network. White squares correspond to regions of interest highlighted in panes b) to f). The colors of the streams correspond to the Strahler order of the network. b) Zoom at the outlet of the basin, where an important portion of the human and infrastructure losses took place. c) Zoom at La Margarita settlement also affected by the flash flood. d) to f) Zoom at key locations along the principal stream. Observed flood spots are shown in blue polygons and model flood spots in red to white grids.

formation of soil type, land use and real-time hydrometeorological data, La Liboriana case implies a challenge for flash flood prediction, modeling and, consequently, risk management. The present paper introduces a hydrologic model-based approach and an integral graphical analysis tool (an integrated spatiotemporal analysis of rainfall evolution, together with soil storages in the basin), not only to simulate and understand all the relevant soil-rainfall-discharge processes that led to the 2015 Salgar flash flood while assessing the associated natural hazards, but also to propose it as a radar QPE-based landslide and flash flood guidance low-cost tool for basins with scarce data and regions with limited resources.

625

The methodology implies the development of a distributed hydrologic model with the capabilities of tracking independently convective and stratiform precipitation within the model as well as keeping track of the runoff and subsurface portions of the streamflow, coupling a shallow landslide submodel and a one-dimensional flash flood scheme (HydroFlash). The model proposed here indeed 630 allows studying the different hydrological processes relevant to flash flood and landslide occurrence by using different simulation resources, serving as the basis for a better understanding of the over-

all basin response. This overall approach helps to isolate flood generating mechanisms or causative factors both in time and also in space, focusing on the important physical processes and not only on statistics (Klemes, 1993; Merz and Blöschl, 2003). It is hoped that knowledge improvement leads to 635 the anticipation of the warning and response by risk management entities.

The evolution of the simulation of Events 1 and 2 show evidence of remarkable behavioral differences. During Event 1 both gravitational and capillary tanks are filled along and across the basin as a result of the quasi-homogeneous rainfall spatial distribution. The return flow is low, and most 640 of the runoff occurs within the first 20 groups (40% of the watershed closest to the outlet). In the period between both events, there is a recession in the capillary and gravitational storages in the entire basin. Capillary storage decays considerably slower than gravitational storage. During Event 2, the flash flood triggering event, the first convective core saturates both capillary and gravitational 645 storages in the upper part of the basin and generates both return flow and significant runoff. Due to soil saturation, the second convective core results mainly in surface runoff. During this event, runoff is generated the lower part of the basin while extreme runoff rates are evident in the upper part of the basin, collocated with the steeper slopes. On the other hand, subsurface flow is more important in magnitude than runoff describing Event 1, while runoff is more relevant for Event 2. The precedent storage and the presence of thunderstorm training profoundly condition the streamflow during Event 650 2. The overall evidence suggests that precedent capillary moisture in the basin plays an essential role in modulating river discharge. This behavior could be linked to the temporal occurrence and relative importance and timing of stratiform and convective formations previously described.

While convective and stratiform partitioning could influence the runoff and subsurface flow separation, the spatial distribution of rainfall relative to watershed network morphometry structure impose a condition on the hydrological response of the basin. In other words, hydrograph formation is not only determined by the rainfall accumulation or maximum intensity, but also by its spatial structure. The structure of the rainfall associated with La Liboriana event highlights the need to consider 655 in more detail the role of orographic rainfall intensification in practical applications such as early warning systems. Evidence suggests the spatial structure of the rainfall is at least as important as the geomorphological features of the basin regulating the generation of flash flood events.

An integrated spatiotemporal analysis of rainfall evolution, together with soil storages in the basin is necessary to study the relevance of antecedent conditions and precipitation type, intensity, and 665 location in the generation of flash flood events. Event 1 increased the overall soil moisture with an associated decrease on infiltration rates similar to results reported by Penna et al. (2011) and Zehe et al. (2010), low infiltration increase runoff rates, which finally affects the susceptibility of the basin to flash floods occurrence (Wagner et al., 1999; Penna et al., 2011; Tramblay et al., 2012). La

Liboriana geomorphological characteristics, corresponding to a steep tropical basin, determine the potential energy that controls water transit velocity. Water tends to reach faster the channels in order 1 and 2 hills, and, at the same time, the sediment production and transport in these hills tend to be larger. Order 3 sub-basins most likely act as transport elements, with no important energy losses. Floods tend to occur in order 4 and 5 sub-basins due to the widening of the channel and slope attenuation.

675

Different authors have focused on trying to understand the general causative factors behind the occurrence of flash floods finding similar to our results, a significant role of basing geomorphology, orography and local convection. For example, Lehmann and Or (2012), using a shallow landslide model, finds an important role of the topography and the rainfall conditions. Turkington et al. (2014) shows how intense locally driven convection appears to be the main meteorological trigger for flash occurrence in the French Alpes. Camarasa-Belmonte (2016) shows how rainfall intensity and duration influences the shape of the hydrograph, with intense rainfall shortening the response time of the basin, and large durations increasing the flood peak. In the Mediterranean region, Boudou et al. (2016) states that in addition to the rainfall, geomorphological characteristics and antecedent soil conditions are key in the generation of flash flooding.

However useful, the evidence in this work only takes into account two successive events; an analysis of more cases and different spatial scales (different basins) would provide robust conclusions in this direction. It is clear that it is not conclusive enough to focus on a single extreme event, rather than on a spectrum of floods Merz and Blöschl (2003). The model simulation results suggest it is imperative to study in depth the long-term link between the relative basin and drainage network orientation and the preferred path of precipitation events and its role in defining the frequency of flash flood occurrence. A better understanding of the network-hills-preferential rainfall advection structure could provide information about basins prone to flash floods when information is scarce.

695

## 6 Conclusions

Extreme rainfall events such as the one that triggered La Liboriana tragedy frequently take place in Colombia and the entire global tropical belt over ungauged basins, often triggering flash floods and torrential flows, endangering vulnerable communities due to poor long-term planning and lack of functional early warning systems. There is a global need for better knowledge and understanding of the hydrological and meteorological conditions that, combined, lead to the manifestation of natural hazards. Such understanding must result in useful practical applications that improve risk management practices saving lives. In the current work, we approach the problem from a hydrolog-

ical modeling point of view, trying, despite the data limitations and the uncertainty of the results, to  
705 shed some light in the first-order processes that modulate the occurrence of flash floods in the region.

In the case of La Liboriana flash flood, radar reflectivity fields were available from a C-Band radar  
operated by the Early Warning System of Medellín and its metropolitan area as part of a local risk  
management strategy. While the municipality of Salgar is located far outside Medellín's metropolitan  
710 area, the radar is about 90 km away from Salgar, and the reflectivity retrievals enable the classification  
of precipitation fields into convective and stratiform areas using widely accepted methodologies  
by the meteorological community. Radar reflectivity is also a proxy for precipitation allowing a quan-  
titative estimation of rainfall fields. This estimation was used together with the hydrologic model to  
assess the different basin-wide processes taking place during the flash flood triggering rainfall event.  
715 The limitations of the methodology presented in this work do not allow to represent all the detailed  
small-scale preferential pathways of water in the watershed, but rather focus on the first-order ap-  
proximation to study the partitioning between runoff vs. subsurface flow. Also, the model results are  
used to obtain a conceptual idea about the general processes, but it must be taken into account that  
the simulations are subject to a calibration process that could lead to erroneous conclusions about the  
720 physical processes. This could be true even as different steps were taken trying to avoid this situation.

The overall model simulation methodology reproduces considerably well the magnitude and tim-  
ing of La Liboriana flash flood discharge peak, showing robustness to changes in the most important  
model parameters, and reasonably well the areas of regional land-slide occurrence and flood spots  
725 location. Model simulation results indicate that the flash-flood and the regional land-slide features  
were strongly influenced by the observed antecedent rainfall associated with a northeasterly strati-  
form event that recharged the gravitational and capillary storages in the entire basin. The hydrologic  
simulation shows that the antecedent event set wet conditions in the entire basin before the oc-  
currence of the flash flood event, governing the streamflow during the latter. Results of the model  
730 simulation also suggest that the first of the two successive convective cores (thunderstorm training)  
over the same region during the second precipitation event (the flash flood event) saturated both  
capillary and gravitational storages in the upper part of the basin and generated both return flow and  
significant runoff. The second convective core resulted mainly in surface runoff spatially collocated  
with the steeper slopes, generating the kinetic energy needed to produce La Liboriana flash flood.  
735 Overall results also show a good agreement between the simulated flood spots and the observed  
ones; this in spite of the limitations imposed by the resolution of the DEM used for extracting cross  
sections, and the model oversimplifications.

Considering all the shortcomings and generalizations, the described model-based approach is po-  
740 tentially useful to assess flood generating mechanisms and as a tool for policy-makers, not only for

short-term decisions in the context of an early warning system but also as a planning resource for long-term risk management. While several improvements need to be implemented, including a better representation of hydraulic parameters, and a direct link between landslides and flood spots similar to the strategy presented in the STEP-TRAMM model (Fan et al., 2017), the results suggest it is  
745 possible to use low-cost methodologies such as the one introduced here as a risk management tool in countries and regions with scarce resources.

## 7 Acknowledgements

This work was supported by SIATA (Sistema de Alerta Temprana de Medellín y el Valle de Aburrá)  
750 funds provided by Área Metropolitana del Valle de Aburrá (AMVA), Municipio de Medellín, Grupo EPM, and ISAGEN under the Research and Technology Contract CD511, 2017. Universidad Nacional de Colombia partly funded Nicolás Velásquez under the Facultad de Minas graduate scholarship program. Both authors would like to thank anonymous reviewer 1 for the detailed and insightful comments that helped to clarify and highlight the message of this work. Both authors also thank Dr.  
755 Eric Gaume, reviewer 2, for his thoughtful comments.

For the technically inclined reader, the hydrologic model and sub-models are written in Fortran 90, and the interface to the model, pre-process, and post-process tools are in python 2.7. The Fortran code is warped to python using **f2py** (Peterson, 2009) and it is publicly available under the Water-  
760 shed Modelling Framework **WMF** in a web repository ([GitHub](#)).

## References

Adamovic, M., Branger, F., Braud, I., and Kralisch, S.: Development of a data-driven semi-distributed hydrological model for regional scale catchments prone to Mediterranean flash floods, *Journal of Hydrology*, 541, 173–189, doi:10.1016/j.jhydrol.2016.03.032, <http://dx.doi.org/10.1016/j.jhydrol.2016.03.032>, 2016.

765 Aristizábal, E., Vélez, J. I., Martínez, H. E., and Jaboyedoff, M.: SHIA\_Landslide: a distributed conceptual and physically based model to forecast the temporal and spatial occurrence of shallow landslides triggered by rainfall in tropical and mountainous basins, *Landslides*, 13, 497–517, doi:10.1007/s10346-015-0580-7, 2016.

770 Aronica, G. T., Brigandí, G., and Morey, N.: Flash floods and debris flow in the city area of Messina, north-east part of Sicily, Italy in October 2009: The case of the Giampilieri catchment, *Natural Hazards and Earth System Science*, 12, 1295–1309, doi:10.5194/nhess-12-1295-2012, 2012.

ASF, J.: Dataset: ASF DAAC 2015, ALOS PALSAR Radiometric Terrain Corrected high res; Includes Material JAXA/METI 2007, doi:10.5067/Z97HFCNKR6VA, <https://vertex.daac.asf.alaska.edu/>, 2011.

775 Ayalew, T. B., Krajewski, W. F., and Mantilla, R.: Connecting the power-law scaling structure of peak-discharges to spatially variable rainfall and catchment physical properties, *Advances in Water Resources*, 71, 32–43, doi:10.1016/j.advwatres.2014.05.009, <http://dx.doi.org/10.1016/j.advwatres.2014.05.009>, 2014.

Berne, A. and Krajewski, W.: Radar for hydrology: Unfulfilled promise or unrecognized potential?, *Advances in Water Resources*, 51, 357 – 366, doi:<https://doi.org/10.1016/j.advwatres.2012.05.005>, <http://www.sciencedirect.com/science/article/pii/S0309170812001157>, 35th Year Anniversary Issue, 2013.

780 Beven, K.: Kinematic subsurface stormflow, *Water Resources Research*, 17, 1419–1424, doi:10.1029/WR017i005p01419, 1981.

Beven, K.: Towards integrated environmental models of everywhere: uncertainty, data and modelling as a learning process, *Hydrology and Earth System Sciences*, 11, 460–467, doi:10.5194/hess-11-460-2007, <http://www.hydrol-earth-syst-sci.net/11/460/2007/>, 2007.

785 Bisht, S., Chaudhry, S., Sharma, S., and Soni, S.: Assessment of flash flood vulnerability zonation through Geospatial technique in high altitude Himalayan watershed, Himachal Pradesh India, *Remote Sensing Applications: Society and Environment*, 12, 35–47, doi:10.1016/j.rsase.2018.09.001, <https://doi.org/10.1016/j.rsase.2018.09.001>, 2018.

790 Blöschl, G., Sivapalan, M., Wagener, T., Viglione, A., and Savenije, H.: Runoff Prediction in Ungauged Basins, in: *Runoff Prediction in Ungauged Basins: Synthesis across Processes, Places and Scales*, edited by Blöschl, G., Sivapalan, M., Wagener, T., Viglione, A., and Savenije, H., Cambridge University Press, Cambridge, [https://www.cambridge.org/core/books/runoff-prediction-in-ungauged-basins/A5DFE99C3CA857127C4C03C6C20032EE](https://www.cambridge.org/core/books/runoff-prediction-in-ungauged-basins/runoff-prediction-in-ungauged-basins/A5DFE99C3CA857127C4C03C6C20032EE), 2012.

795 Bonell, M., McDonnell, J. J., Scatena, F. N., Seibert, J., Uhlenbrook, S., and van Lanen, H. A. J.: HELP-ing FRIENDs in PUBs: Charting a course for synergies within international water research programmes in gauged and ungauged basins, *Hydrological Processes*, 20, 1867–1874, doi:10.1002/hyp.6196, 2006.

Borga, M., Anagnostou, E. N., Blöschl, G., and Creutin, J. D.: Flash flood forecasting, warning and risk management: The HYDRATE project, *Environmental Science and Policy*, 14, 834–844, 800 doi:10.1016/j.envsci.2011.05.017, 2011.

Boudou, M., Lang, M., Vinet, F., and C??ur, D.: Comparative hazard analysis of processes leading to remarkable flash floods (France, 1930??1999), *Journal of Hydrology*, 541, 533–552, doi:10.1016/j.jhydrol.2016.05.032, <http://dx.doi.org/10.1016/j.jhydrol.2016.05.032>, 2016.

Camarasa-Belmonte, A. M.: Flash floods in Mediterranean ephemeral streams in Valencia Region (Spain), 805 *Journal of Hydrology*, doi:10.1016/j.jhydrol.2016.03.019, 2016.

Castillo, V. M., Gómez-Plaza, A., and Martínez-Mena, M.: The role of antecedent soil water content in the runoff response of semiarid catchments: A simulation approach, *Journal of Hydrology*, 284, 114–130, doi:10.1016/S0022-1694(03)00264-6, 2003.

Dhakal, A. S. and Sidle, R. C.: Distributed simulations of landslides for different rainfall conditions, *Hydrological Processes*, 18, 757–776, doi:10.1002/hyp.1365, 2004.

Douinot, A., Roux, H., Garambois, P. A., Larnier, K., Labat, D., and Dartus, D.: Accounting for rainfall systematic spatial variability in flash flood forecasting, *Journal of Hydrology*, 541, 359–370, doi:10.1016/j.jhydrol.2015.08.024, <http://dx.doi.org/10.1016/j.jhydrol.2015.08.024>, 2016.

Duan, Q., Schaake, J., Andreassian, V., Franks, S., Goteti, G., Gupta, H., Gusev, Y., Habets, F., Hall, a., Hay, 815 L., Hogue, T., Huang, M., Leavesley, G., Liang, X., Nasonova, O., Noilhan, J., Oudin, L., Sorooshian, S., Wagener, T., and Wood, E.: Model Parameter Estimation Experiment (MOPEX): An overview of science strategy and major results from the second and third workshops, *Journal of Hydrology*, 320, 3–17, doi:10.1016/j.jhydrol.2005.07.031, 2006.

Fan, L., Lehmann, P., McArdell, B., and Or, D.: Linking rainfall-induced landslides with debris flows runout patterns towards catchment scale hazard assessment, *Geomorphology*, 280, 1–15, 820 doi:10.1016/j.geomorph.2016.10.007, <http://dx.doi.org/10.1016/j.geomorph.2016.10.007>, 2017.

Foster G.R., Huggins L.F., M. L.: A Laboratory Study of Rill Hydraulics: I. Velocity Relationships, *American Society of Agricultural and Biological Engineers*, 3, 0790–0796, doi:10.13031/2013.32873, 1984.

Fragoso, M., Trigo, R. M., Pinto, J. G., Lopes, S., Lopes, a., Ulbrich, S., and Magro, C.: The 20 February 2010 825 Madeira flash-floods: Synoptic analysis and extreme rainfall assessment, *Natural Hazards and Earth System Science*, 12, 715–730, doi:10.5194/nhess-12-715-2012, 2012.

Francés, F., Vélez, J. I., and Vélez, J. J.: Split-parameter structure for the automatic calibration of distributed hydrological models, *Journal of Hydrology*, 332, 226–240, doi:10.1016/j.jhydrol.2006.06.032, 2007a.

Francés, F., Vélez, J. I., and Vélez, J. J.: Split-parameter structure for the automatic calibration of distributed 830 hydrological models, *Journal of Hydrology*, 332, 226–240, doi:10.1016/j.jhydrol.2006.06.032, 2007b.

Garambois, P. a., Roux, H., Larnier, K., Castaings, W., and Dartus, D.: Characterization of process-oriented hydrologic model behavior with temporal sensitivity analysis for flash floods in Mediterranean catchments, *Hydrology and Earth System Sciences*, 17, 2305–2322, doi:10.5194/hess-17-2305-2013, 2013.

Golden, L. A. and Springer, G. S.: Channel geometry, median grain size, and stream power in small mountain 835 streams, *Geomorphology*, 78, 64–76, doi:10.1016/j.geomorph.2006.01.031, 2006.

Gruntfest, E. and Handmer, J.: Coping with Flash Floods, NATO science series. Partnership sub-series 2, Environmental security, Springer Netherlands, <https://books.google.com.co/books?id=pwsczTbbY9sC>, 2001.

Hardy, J., Gourley, J. J., Kirstetter, P. E., Hong, Y., Kong, F., and Flamig, Z. L.: A method for probabilistic flash flood forecasting, *Journal of Hydrology*, 541, 480–494, doi:10.1016/j.jhydrol.2016.04.007, <http://dx.doi.org/10.1016/j.jhydrol.2016.04.007>, 2016.

Houze, R.: Mesoscale convective systems, *Reviews of Geophysics*, 42, doi:10.1029/2004RG000150, <https://agupubs.onlinelibrary.wiley.com/doi/abs/10.1029/2004RG000150>, 2004.

Houze, R. A.: Observed structure of mesoscale convective systems and implications for large-scale heating, *Quarterly Journal of the Royal Meteorological Society*, 115, 425–461, doi:10.1002/qj.49711548702, 1989.

845 Houze, R. A., Rasmussen, K. L., Zuluaga, M. D., and Brodzik, S. R.: The variable nature of convection in the tropics and subtropics: A legacy of 16 years of the Tropical Rainfall Measuring Mission satellite, *Reviews of Geophysics*, 53, 994–1021, doi:10.1002/2015RG000488, 2015.

Jonkman, S.: Global perspectives on loss of human life caused by floods, *NATURAL HAZARDS*, 34, 151–175, doi:10.1007/s11069-004-8891-3, 2005.

850 Kahana, R., Ziv, B., Enzel, Y., and Dayan, U.: Synoptic climatology of major floods in the Negev Desert, Israel, *International Journal of Climatology*, 22, 867–882, doi:10.1002/joc.766, 2002.

Khosravi, K., Pham, B. T., Chapi, K., Shirzadi, A., Shahabi, H., Revhaug, I., Prakash, I., and Tien Bui, D.: A comparative assessment of decision trees algorithms for flash flood susceptibility modeling at Haraz watershed, northern Iran, *Science of the Total Environment*, 627, 744–755, doi:10.1016/j.scitotenv.2018.01.266, 855 <https://doi.org/10.1016/j.scitotenv.2018.01.266>, 2018.

Kirkby, M. J. and Chorley, R. J.: Throughflow, Overland Flow and Erosion, *International Association of Scientific Hydrology. Bulletin*, 12, 5–21, doi:10.1080/02626666709493533, <http://www.tandfonline.com/doi/abs/10.1080/02626666709493533>, 1967.

Klemes, V.: Probability of extreme hydrometeorological events—A different approach, in *Extreme Hydrological Events: Precipitation, Floods and Droughts*, IAHS Publ, 1993.

860 Kubota, J. and Sivapalan, M.: Towards a Catchment-Scale Model of Subsurface Small-Scale Process-Based Modelling and Runoff Generation Based on Synthesis of Field Studies, *Hydrological Processes*, 9, 541–554, 1995.

Lehmann, P. and Or, D.: Hydromechanical triggering of landslides: From progressive local failures to mass release, *Water Resources Research*, 48, 1–24, doi:10.1029/2011WR010947, 2012.

865 Leopold, L.B., M. T.: The hydraulic geometry of stream channels and some physiographic implications, *Geological survey professional paper*, 1953.

Llasat, M. C., Marcos, R., Turco, M., Gilabert, J., and Llasat-Botija, M.: Trends in flash flood events versus convective precipitation in the Mediterranean region: The case of Catalonia, *Journal of Hydrology*, 541, 870 24–37, doi:10.1016/j.jhydrol.2016.05.040, <http://dx.doi.org/10.1016/j.jhydrol.2016.05.040>, 2016.

Longoni, L., Ivanov, V. I., Brambilla, D., Radice, A., and Papini, M.: Analysis of the temporal and spatial scales of soil erosion and transport in a Mountain Basin, *Italian Journal of Engineering Geology and Environment*, 16, 17–30, doi:10.4408/IJEGE.2016-02.O-02, 2016.

875 Mapes, B., Warner, T., Xu, M., and Negri, A. J.: Diurnal Patterns of Rainfall in Northwestern South America. Part I: Observations and Context, *Monthly Weather Review*, 131, 799–812, doi:10.1175/1520-0493(2003)131<0799:DPORIN>2.0.CO;2, [https://doi.org/10.1175/1520-0493\(2003\)131<0799:DPORIN>2.0.CO;2](https://doi.org/10.1175/1520-0493(2003)131<0799:DPORIN>2.0.CO;2), 2003.

Marchi, L., Cavalli, M., Amponsah, W., Borga, M., and Crema, S.: Upper limits of flash flood stream power in Europe, *Geomorphology*, 272, 68–77, doi:10.1016/j.geomorph.2015.11.005, <http://dx.doi.org/10.1016/j.geomorph.2015.11.005>, 2016.

880

Marra, F., Destro, E., Nikolopoulos, E. I., Zoccatelli, D., Dominique Creutin, J., Guzzetti, F., and Borga, M.: Impact of rainfall spatial aggregation on the identification of debris flow occurrence thresholds, *Hydrology and Earth System Sciences*, 21, 4525–4532, doi:10.5194/hess-21-4525-2017, 2017.

Martín-Vide, J. P. and Llasat, M. C.: The 1962 flash flood in the Rubí stream (Barcelona, Spain), *Journal of Hydrology*, 566, 441–454, doi:10.1016/j.jhydrol.2018.09.028, <https://doi.org/10.1016/j.jhydrol.2018.09.028>, 2018.

885 Merz, R. and Blöschl, G.: A process typology of regional floods, *Water Resources Research*, 39, 1–20, doi:10.1029/2002WR001952, <http://doi.wiley.com/10.1029/2002WR001952>, 2003.

Norbiato, D., Borga, M., Degli Esposti, S., Gaume, E., and Anquetin, S.: Flash flood warning based on rainfall 890 thresholds and soil moisture conditions: An assessment for gauged and ungauged basins, *Journal of Hydrology*, pp. 274–290, doi:10.1016/j.jhydrol.2008.08.023, 2008.

Obrien, J.S., J. P.: Laboratory analysis of mudflow properties, *Journal of Hydrological Engineering*, 8, 877–887, 1988.

Osorio, H.G., A. S.: Unidades de suelo representativas de la zona cafetera de Colombia, *Federación de Cafeteros 895 de Colombia*, 2008.

Ozturk, U., Wendi, D., Crisologo, I., Riemer, A., Agarwal, A., Vogel, K., López-Tarazón, J. A., and Korup, O.: Rare flash floods and debris flows in southern Germany, *Science of the Total Environment*, 626, 941–952, doi:10.1016/j.scitotenv.2018.01.172, 2018.

Penna, D., Tromp-Van Meerveld, H. J., Gobbi, a., Borga, M., and Dalla Fontana, G.: The influence of soil 900 moisture on threshold runoff generation processes in an alpine headwater catchment, *Hydrology and Earth System Sciences*, 15, 689–702, doi:10.5194/hess-15-689-2011, 2011.

Peterson, P.: F2PY: a tool for connecting Fortran and Python programs, *International Journal of Computational Science and Engineering*, 4, 296, doi:10.1504/IJCSE.2009.029165, <http://www.inderscience.com/link.php?id=29165>, 2009.

905 Poveda, G. and Mesa, O. J.: On the existence of Lloró (the雨iest locality on Earth): Enhanced ocean-land-atmosphere interaction by a low-level jet, *Geophysical Research Letters*, 27, 1675–1678, doi:10.1029/1999GL006091, <https://agupubs.onlinelibrary.wiley.com/doi/abs/10.1029/1999GL006091>, 2000.

Poveda, G., Vélez, J. I., Mesa, O. J., Cuartas, A., Barco, J., Mantilla, R. I., Mejía, J. F., Hoyos, C. D., Ramírez, 910 J. M., Ceballos, L. I., Zuluaga, M. D., Arias, P. a., Botero, B. a., Montoya, M. I., Giraldo, J. D., and Quevedo, D. I.: Linking Long-Term Water Balances and Statistical Scaling to Estimate River Flows along the Drainage Network of Colombia, *Journal of Hydrologic Engineering*, 12, 4–13, doi:10.1061/(ASCE)1084-0699(2007)12:1(4), 2007.

Rennó, C. D., Nobre, A. D., Cuartas, L. A., Soares, J. V., Hodnett, M. G., Tomasella, J., and Waterloo, M. J.: HAND, a new terrain descriptor using SRTM-DEM: Mapping terra-firme rainforest environments in Amazonia, *Remote Sensing of Environment*, 112, 3469–3481, doi:10.1016/j.rse.2008.03.018, <http://linkinghub.elsevier.com/retrieve/pii/S003442570800120X>, 2008.

Rodríguez-Blanco, M., Taboada-Castro, M., and Taboada-Castro, M.: Rainfall-runoff response and event-based runoff coefficients in a humid area (northwest Spain), *Hydrological Sciences Journal*, 403, 319–329,

920 doi:10.1080/02626669509491418, <http://www.tandfonline.com/action/journalInformation?journalCode=thsj20>{%}0A<http://www.tandfonline.com/action/journalInformation?journalCode=thsj20>, 2012.

Roux, H., Labat, D., Garambois, P. A., Maubourgues, M. M., Chorda, J., and Dartus, D.: A physically-based parsimonious hydrological model for flash floods in Mediterranean catchments, *Natural Hazards and Earth System Science*, 11, 2567–2582, doi:10.5194/nhess-11-2567-2011, 2011.

925 Ruiz-Villanueva, V., Díez-Herrero, A., Bodoque, J. M., Ballesteros Cánovas, J. A., and Stoffel, M.: Characterisation of flash floods in small ungauged mountain basins of Central Spain using an integrated approach, *Catena*, 110, 32–43, doi:10.1016/j.catena.2013.06.015, <http://dx.doi.org/10.1016/j.catena.2013.06.015>, 2013.

Šálek, M., Brezková, L., and Novák, P.: The use of radar in hydrological modeling in the Czech Republic – 930 case studies of flash floods, *Natural Hazards and Earth System Science*, 6, 229–236, doi:10.5194/nhess-6-229-2006, 2006.

Savage, S. B. and Sayed, M.: Stresses developed by dry cohesionless granular materials sheared in an annular shear cell, *Journal of Fluid Mechanics*, 142, 391–430, doi:10.1017/S0022112084001166, 1984.

Schumacher, R. S. and Johnson, R. H.: Organization and Environmental Properties of Extreme-Rain-Producing 935 Mesoscale Convective Systems, *Monthly Weather Review*, 133, 961–976, doi:10.1175/MWR2899.1, <http://journals.ametsoc.org/doi/abs/10.1175/MWR2899.1>, 2005.

Seibert, J. and Beven, K. J.: Gauging the ungauged basin : how many discharge measurements are needed?, *Hydrology and Earth System Sciences*, 13, 883–892, doi:10.5194/hessd-6-2275-2009, <http://www.hydrol-earth-syst-sci.net/13/883/2009/>, 2009.

940 Serra, J.: *Image Analysis and Mathematical Morphology*, Academic Press, Inc., Orlando, FL, USA, 1983.

Sidle, R., Gomi, T., and Tsukamoto, Y.: Discovery of zero-order basins as an important link for progress in hydrogeomorphology, *Hydrological Processes*, pp. 1–7, doi:10.1002/hyp.13246, <http://doi.wiley.com/10.1002/hyp.13246>, 2018.

945 Sivapalan, M., Takeuchi, K., FRANKS, S. W., GUPTA, V. K., KARAMBIRI, H., LAKSHMI, V., LIANG, X., McDONNELL, J. J., MENDIONDO, E. M., J, P. E. O., OKI, T., POMEROY, J. W., SCHERTZER, D., UHLENBROOK, S., and E. ZEHE: IAHS Decade on Predictions in Ungauged Basins (PUB), 2003–2012: Shaping an exciting future for the hydrological sciences, *Hydrological Sciences Journal*, pp. 857–880, doi:10.1080/02626667.2015.1131899, <http://www.tandfonline.com/action/journalInformation?journalCode=thsj20>{%}5Cn<http://dx.doi.org/10.1080/02626667.2015.1131899>, 2016.

950 Steiner, M., Houze, R. a., and Yuter, S. E.: Climatological Characterization of Three-Dimensional Storm Structure from Operational Radar and Rain Gauge Data, doi:10.1175/1520-0450(1995)034<1978:CCOTDS>2.0.CO;2, <http://papers3://publication/uuid/D11C9905-6CE2-40B5-8A93-5E5300EB3A6E>, 1995.

Takahashi, T.: *Debris flow*, Taylor y francis, 2 edn., 1991.

955 Tramblay, Y., Bouaicha, R., Brocca, L., Dorigo, W., Bouvier, C., Camici, S., and Servat, E.: Estimation of antecedent wetness conditions for flood modelling in northern Morocco, *Hydrology and Earth System Sciences*, 16, 4375–4386, doi:10.5194/nhess-16-4375-2012, 2012.

960 Turkington, T., Ettema, J., Van Westen, C. J., and Breinl, K.: Empirical atmospheric thresholds for debris flows and flash floods in the southern French Alps, *Natural Hazards and Earth System Sciences*, 14, 1517–1530, doi:10.5194/nhess-14-1517-2014, 2014.

965 Vannier, O., Anquetin, S., and Braud, I.: Investigating the role of geology in the hydrological response of Mediterranean catchments prone to flash-floods: Regional modelling study and process understanding, *Journal of Hydrology*, 541, 158–172, doi:10.1016/j.jhydrol.2016.04.001, <http://dx.doi.org/10.1016/j.jhydrol.2016.04.001>, 2016.

970 Vélez, J.: Desarrollo de un modelo hidrológico conceptual y distribuido orientado a la simulación de crecidas, Tesis doctoral - Universidad Politécnica de Valencia, p. 266, 2001.

975 Wagener, T., Gupta, H., Yatheendradas, S., Goodrich, D., Unkrich, C., and Schaffner, M.: Understanding sources of uncertainty in flash-flood forecasting for semi-arid regions., *IAHS Publication* 313, pp. 204–212, 2007.

980 Wagner, W., Lemoine, G., and Rott, H.: A method for estimating soil moisture from ERS Scatterometer and soil data, *Remote Sensing of Environment*, 70, 191–207, doi:10.1016/S0034-4257(99)00036-X, 1999.

985 Wu, W. and Sidle, R. C.: and Number Values Agreed Closely With, *Water Resources*, 31, 2097–2110, doi:10.1029/95WR01136, 1995.

Yamanaka, T. and Ma, W.: Runoff prediction in a poorly gauged basin using isotope-calibrated models, *Journal of Hydrology*, 544, 567–574, doi:10.1016/j.jhydrol.2016.12.005, <http://dx.doi.org/10.1016/j.jhydrol.2016.12.005>, 2017.

Yatheendradas, S., Wagener, T., Gupta, H., Unkrich, C., Goodrich, D., Schaffner, M., and Stewart, A.: Understanding uncertainty in distributed flash flood forecasting for semiarid regions, *Water Resources Research*, 44, 1–17, doi:10.1029/2007WR005940, 2008.

Younis, J., Anquetin, S., and Thielen, J.: The benefit of high-resolution operational weather forecasts for flash flood warning, *Hydrology and Earth System Sciences Discussions*, 5, 345–377, doi:10.5194/hessd-5-345-2008, 2008.

Zehe, E., Graeff, T., Morgner, M., Bauer, A., and Bronstert, A.: Plot and field scale soil moisture dynamics and subsurface wetness control on runoff generation in a headwater in the Ore Mountains, *Hydrology and Earth System Sciences*, 14, 873–889, doi:10.5194/hess-14-873-2010, 2010.